Monthly Notices
of the
ROYAL ASTRONOMICAL SOCIETY

MNRAS **527,** 8793–8811 (2024)
Advance Access publication 2023 November 29

https://doi.org/10.1093/mnras/stad3703

INSPIRE: INvestigating Stellar Population In RElics – V. A catalogue of ultra-compact massive galaxies outside the local Universe and their degree of relicness

C. Spiniello,[1,2★] G. D'Ago,[2,3] L. Coccato,[4] J. Hartke,[5,6] C. Tortora,[2] A. Ferré-Mateu,[7,8] C. Pulsoni,[9] M. Cappellari,[1] M. Maksymowicz-Maciata,[1] M. Arnaboldi,[4] D. Bevacqua,[10,11] A. Gallazzi,[12] L. K. Hunt,[12] F. La Barbera,[2] I. Martín-Navarro,[7,8] N. R. Napolitano,[13] M. Radovich,[14] P. Saracco,[15] D. Scogniamiglio,[16] M. Spavone[2] and S. Zibetti[12]

[1] *Sub-Department of Astrophysics, Department of Physics, University of Oxford, Denys Wilkinson Building, Keble Road, Oxford OX1 3RH, UK*
[2] *INAF - Osservatorio Astronomico di Capodimonte, Via Moiariello 16, I-80131 Naples, Italy*
[3] *Institute of Astronomy, University of Cambridge, Madingley Road, Cambridge CB3 0HA, UK*
[4] *European Southern Observatory, Karl-Schwarzschild-Straße 2, D-85748 Garching, Germany*
[5] *Finnish Centre for Astronomy with ESO (FINCA), University of Turku, FI-20014 Turku, Finland*
[6] *Tuorla Observatory, Department of Physics and Astronomy, University of Turku, FI-20014 Turku, Finland*
[7] *Instituto de Astrofísica de Canarias, Vía Láctea s/n, E-38205 La Laguna, Tenerife, Spain*
[8] *Departamento de Astrofisica, Universidad de La Laguna, E-38200 La Laguna, Tenerife, Spain*
[9] *Max-Planck-Institut für extraterrestrische Physik, Giessenbachstrasse, D-85748 Garching, Germany*
[10] *INAF - Osservatorio Astronomico di Brera, via Brera 28, I-20121 Milano, Italy*
[11] *DiSAT, Università degli Studi dell'Insubria, via Valleggio 11, I-22100 Como, Italy*
[12] *INAF - Osservatorio Astrofisico di Arcetri, Largo Enrico Fermi5, I-50125 Firenze, Italy*
[13] *School for Physics and Astronomy, Sun Yat-sen University, Guangzhou 519082, Zhuhai Campus, China*
[14] *INAF - Osservatorio astronomico di Padova, Vicolo Osservatorio 5, I-35122 Padova, Italy*
[15] *INAF - Osservatorio Astronomico di Brera, via Brera 28, I-20121 Milano, Italy*
[16] *Jet Propulsion Laboratory, California Institute of Technology, 4800, Oak Grove Drive Pasadena, CA 91109, USA*

Accepted 2023 November 27. Received 2023 November 27; in original form 2023 August 25

ABSTRACT

This paper presents the third data release of the INvestigating Stellar Population In RElics (INSPIRE) project, comprising 52 ultra-compact massive galaxies (UCMGs) observed with the X-Shooter spectrograph. We measure integrated stellar velocity dispersion, [Mg/Fe] abundances, ages, and metallicities for all the `INSPIRE` objects. We thus infer star formation histories and confirm the existence of a *degree of relicness* (DoR), defined in terms of the fraction of stellar mass formed by $z = 2$, the time at which a galaxy has assembled 75 per cent of its mass, and the final assembly time. Objects with a high DoR assembled their stellar mass at early epochs, while low-DoR objects show a non-negligible fraction of later formed populations and hence a spread in ages and metallicities. A higher DoR correlates with larger [Mg/Fe], supersolar metallicity, and larger velocity dispersion values. The 52 UMCGs span a large range of DoR from 0.83 to 0.06, with 38 of them having formed more than 75 per cent of their mass by $z = 2$. Of these, nine are extreme relics (DoR>0.7), since they formed the totality (> 99 per cent) of their stellar mass by redshift $z = 2$. The remaining 14 UCMGs cannot be considered relics, as they are characterized by more extended star formation histories. With `INSPIRE` we built the first sizeable sample of relics outside the local Universe, up to $z \sim 0.4$, increasing the number of confirmed relics by a factor of >10, and opening up an important window to explain the mass assembly of massive galaxies in the high-z Universe.

Key words: galaxies: elliptical and lenticular, cD – galaxies: evolution – galaxies: formation – galaxies: kinematics and dynamics – galaxies: star formation – galaxies: stellar content.

1 INTRODUCTION

Massive relics (Trujillo et al. 2009) are nearby old ultra-compact massive galaxies (UCMGs) that descend from those high-redshift massive passive compact galaxies (Nanayakkara et al. 2022; Carnall et al. 2023), the so-called 'red nuggets' (Damjanov et al. 2009). According to the two-phase formation scenario (Naab, Johansson & Ostriker 2009; Oser et al. 2010; Naab et al. 2014; Huertas-Company et al. 2016), red nuggets are formed at high redshift from an intense and fast dissipative series of processes that generate, after star formation (SF) quenches, a massive, passive, and very compact

★ E-mail: chiara.spiniello@physics.ox.ac.uk

galaxy. Then, after this dissipative phase is concluded (at $z \sim 2$, Zolotov et al. 2015), a second phase starts, characterized by gas inflows, dry mergers, and interactions. This accretion phase, which is much more extended in time than the first one, is responsible for the dramatic structural evolution and size growth of early-type galaxies (ETGs) from $z \sim 2$ to today (Buitrago et al. 2018).

As the time-scale for the initial phase is extremely short, observing massive galaxies at such stages is incredibly challenging. However, relics, slipping passively through cosmic time without interacting with any other structure, reached the nearby Universe as compact as they were when they formed and populated only by very ancient stars. Hence, as *relics of the ancient Universe*, they allow us to study the physical processes that shaped the mass assembly of galaxies in the high-z Universe with the amount of details only achievable in the nearby Universe.

Since the discovery and spectroscopic confirmation of three relics in the local Universe (Trujillo et al. 2014; Yıldırım et al. 2015, 2017; Ferré-Mateu et al. 2017), a lot of work has been devoted to the search and confirmation of red UCMGs (e.g. Damjanov et al. 2015a, b; Tortora et al. 2016, 2018; Charbonnier et al. 2017; Scognamiglio et al. 2020). These are the perfect *'bonafide'* relic candidates, having red colours, very small sizes, and large stellar masses.[1] The number density of relics in the local Universe is very small (i.e. $\sim 6 \times 10^{-7}$ Mpc^{-3}, Ferré-Mateu et al. 2017). However, systematic surveys of UCMGs have shown that their number density rises by almost two orders of magnitude between $z = 0$ and $z \sim 0.5$ (Trujillo, Carrasco & Ferré-Mateu 2012; Damjanov et al. 2013, 2014, 2015a; Poggianti et al. 2013; Sanders 2014; Charbonnier et al. 2017; Tortora et al. 2018; Scognamiglio et al. 2020; Lisiecki et al. 2023). This should imply that relics are more common at intermediate redshifts too, and hence, reliable statistical samples can be built at these redshifts. The main goal of the INvestigating Stellar Population In RElics (`INSPIRE`), described in the next section, is, indeed, to build the first statistically large sample of *spectroscopically confirmed relics outside the local Universe*.

The paper is organized as follows. The state of the art in the topic and the current status of the `INSPIRE` project, observations, and previous results are described in Section 2; the data analysis and stellar kinematics are presented in Section 3; and the stellar population analysis is presented in Section 4. The main results, including the relic confirmation and characterization, are presented in Section 5. Finally, we present our conclusions and outline the future development of `INSPIRE` in Section 6.

Throughout the paper, we assume a standard Lambda cold dark matter cosmology with $H_0 = 69.6$ km s^{-1} Mpc^{-1}, $\Omega_\Lambda = 0.714$, and $\Omega_\mathrm{M} = 0.286$ (Bennett et al. 2014).

2 THE INSPIRE PROJECT

`INSPIRE` builds up on a long process dedicated to a systematic census of UCMGs in the redshift range $0.1 < z < 0.4$. First, we carried out a photometric selection of ultra-compact galaxies in the Kilo Degree Survey (KiDS, Kuijken 2011) DR3 footprint (de Jong et al. 2017), leveraging on its exquisite image quality (angular scale of 0.21 arcsec pixel^{-1} and a median r-band seeing of ∼0.65 arcsec, de Jong et al. 2015) and wide-sky coverage (Tortora et al. 2016, 2018). Then, with a multisite and multitelescope spectroscopic follow-up campaign, we confirmed 117 of them, obtaining low signal-to-noise ratio (SNR) and medium-resolution optical spectra from which we infer the redshifts (Tortora et al. 2018; Scognamiglio et al. 2020, hereafter T18 and S20, respectively). However, to finally confirm them as relics of the ancient Universe, it is necessary to constrain their stellar population parameters, demonstrating that the great majority of their stellar mass has assembled at very high redshift through a single, very short SF episode. This is the main goal of the `INSPIRE` Project, which aims at building the first large catalogue of spectroscopically confirmed relics at $0.1 < z < 0.4$. This redshift range represents a positive step forward in bridging the gap between the very small sample of relics in the local Universe with the large population of high-redshift red nuggets.

The `INSPIRE` data have been collected as part of an ESO Large Programme (LP, ID: 1104.B-0370, PI: C. Spiniello) that started in P104 (2019 October) and was completed in 2023 March to obtain high SNR spectra with the X-Shooter spectrograph (XSH, Vernet et al. 2011) of 52 UCMGs at redshift $0.1 < z < 0.4$. These objects all have $g - i$ broad-band colour compatible with that of a stellar population with integrated ages ≥8 Gyr (considering a solar, supersolar, and a subsolar metallicity, see fig. 1 in Spiniello et al. 2021b). They also all have very small sizes (with effective radii $\mathrm{R_e} < 2$ kpc), large stellar masses ($\mathrm{M}_\star > 6 \times 10^{10} \mathrm{M}_\odot$), and are clear outliers in the stellar mass–size plane (see fig. 2 in Spiniello et al. 2021a). Due to high SNR, wide wavelength spectra (covering from the UVB to the NIR), we are able to infer the stellar kinematics and population properties [age, metallicity, elemental abundance, and low-mass end of the initial mass function (IMF) slope] of these UCMGs, hence confirming or refuting their relic nature.

2.1 Previous results

In this section, we summarize the main results previously obtained by `INSPIRE`, which have been presented in previous papers of the series. In Spiniello et al. (2021a), the Pilot Program of the Survey, we have presented several quantitative tests to validate our observational set-up and strategy and our methods to infer kinematics and stellar population parameters. We have also obtained preliminary results on three systems, completely observed during the first semester of observations. With the first data release (Spiniello et al. 2021b, hereafter INSPIRE DR1), we have carried out a precise stellar population analysis for 19 UCMGs. In particular, we have estimated the stellar population ages, metallicities, and [Mg/Fe] abundances from their UVB and VIS spectra. 10 of them have been confirmed as relics (implying a preliminary successful rate for the survey of ∼50 per cent) since they had formed more than 75 per cent of their stellar masses early on in cosmic time through an SF burst.

The third paper of the series (Martín-Navarro et al. 2023) focuses instead on the stellar IMF, hinting at a possible dwarf-rich IMF in relics with respect to non-relics, although larger number statistics will be necessary to confirm this result.

Finally, in DR2 D'Ago et al. (2023, hereafter INSPIRE DR2), the fourth paper of the series, we have performed a detailed stellar kinematic study on 40 objects, focusing on all sources of systematic uncertainties that affect the determination of the integrated stellar velocity dispersion. This quantity might be useful, in the future, as a selection criterion to identify reliable relic candidates. In fact, from DR1, we have shown that, at equal stellar mass, relics (and especially extreme relics) have larger velocity dispersion values than normal-sized ETGs and ultra-compact non-relics. However, this result needs to be confirmed with a larger statistical sample of galaxies.

---

[1] Different works use different thresholds for the stellar mass and the half-light radius. Generally, the low-mass limit is a few times $10^{10}\mathrm{M}_\odot$, and the upper size limit is ∼1.5–2.5 kpc.

In `INSPIRE` DR1, we adopted an operational definition of 'relic' as a way to identify objects that had formed the great majority of their stars at very high z. Now that the `INSPIRE` sample is completed, we move away from this empirical definition and define instead a quantitative number, the 'degree of relicness' (DoR), for all the 52 UCMGs based on their star formation histories (SFHs). As we will discuss in Section 5, the DoR not only provides a useful parameter to quantify how 'extreme' the SFH is, enabling an operative definition of relics, but it also serves as a means to quantify the relative contribution of very old and lately formed (or accreted) stars. Finally, a larger number statistic, which is now achieved, will also allow us to assess whether the DoR correlates with morphological (sizes), photometrical (colours), and structural (boxyness/discyness) properties and/or with the environment in which UCMGs live, and hence shed light on their formation mechanisms.

2.2 Data Release 3: the complete sample

This paper presents the complete INSPIRE sample, comprising 52 UCMGs at $0.1 < z < 0.4$, all with $\mathrm{R_e} < 2$ kpc and $\mathrm{M}_\star > 6 \times 10^{10} \mathrm{M}_\odot$, of which 12 are new and still unpublished. For each UCMG, we have optical and NIR photometry from KiDS and VIKING (Edge, Sutherland & VIKING Team 2014), structural parameters derived in Roy et al. (2018), and stellar masses inferred from SED fitting in the *ugri* bands (T18, S20). In this paper, we add to these morpho-photometric characteristics precise measurements of the stellar velocity dispersion, stellar age, metallicity, and [Mg/Fe] inferred from an integrated spectrum encapsulating 50 per cent of the light (R50, see Section 3 for more info). All these quantities are released as part of a high-value catalogue to the ESO Science Portal.

Table 1 gives a summary of the photometric and structural characteristics of the complete `INSPIRE` sample. These are taken from T18 and S20 and based on the analysis of optical images from the KiDS Survey, as detailed below. Specifically, together with ID and coordinates, we list the INSPIRE Data Release (DR) where the UCMG has been first presented and the sample from which it is drawn. Then, we provide g-, r- and i-band magnitudes, corrected by extinction, the circularized effective radii ($\mathrm{R_e}$), Sérsic index (n), and axis ratio (q). These last three quantities have been calculated as the median of the quantities inferred from g, r, and i images. Measures in each single band are reported in T18 and S20 for all 52 systems. They are obtained by fitting a point spread function (PSF) convolved Sérsic profile to the images using the code 2DPHOT (La Barbera et al. 2008).[2] Uncertainties on the sizes, given the range covered by the `INSPIRE` objects, are of the order of 20 per cent for objects with effective radii larger than 0.2 but rise up to more than 50 per cent for even smaller objects, as visible from fig. B2 in T18. We refer the reader to the same paper, where the quality of these structural parameters is assessed through simulated images. Finally, the last column of the table lists stellar masses, also taken from T18 and S20 and inferred from SED fitting in the *ugri* bands.

Fig. 1 shows 6 arcsec × 6 arcsec cut-outs obtained combining the g, r, and i bands from KiDS images. We note that the astrometry is not perfect in few cases. We have thus realigned the galaxy centres by fitting them with a Gaussian. The galaxies appear all very small and compact on the sky, although in many cases hints of a flattened edge on structure can be seen.[3] Unfortunately, since the PSF of KiDS images is comparable to the sizes of the `INSPIRE` galaxies, it is impossible to obtain a detailed morphological classification. Obtaining photometric data with better spatial sampling and higher resolution, either via AO supported imaging or from space, is the only way to infer more precise structural parameters for these ultra-compact galaxies.

3 DATA ANALYSIS AND STELLAR KINEMATICS

The data reduction and analysis have already been extensively described in previous papers. We refer the readers to `INSPIRE` DR1 and `INSPIRE` DR2 for a complete description and for histograms of the distribution in right ascension (RA), declination (Dec.), redshift, as well as stellar masses, Sérsic indices, and axis ratios. In this final data release (DR3), we add 12 new systems to those already presented in DR1 and DR2, completing the spectroscopic analysis for the 52 galaxies in the `INSPIRE` sample.

We highlight the main steps of the analysis in the following. As in the previous papers, we reduce the data with the standard ESO XSH pipeline (v3.5.3) under the ESO Reflex Workflow (Freudling et al. 2013, version 2.11.3) until the creation of a two-dimensional (2D) spectral frame per each observation block and per each arm of the detector. Then, we extract a one-dimensional (1D) integrated spectrum encapsulating 50 per cent of the light. We obtain in this way an integrated 1D spectrum comparable in light fraction to that extracted at the $\mathrm{R_e}$, but taking into account the seeing during observations. Given the very small apparent sizes of these UCMGs, the spectra are completely seeing-dominated. Hence, we extract the R50 1D spectra starting from the surface brightness profiles of the 2D spectra and then integrating them up to the aperture that encapsulates 50 per cent of the total light but contains a mix of light from inside and outside the real effective radius (we refer the readers to `INSPIRE` DR1 for a more detailed description on the 1D extraction). Finally, we correct the VIS and NIR arms for telluric absorption lines, using the code MOLECFIT[4] (Smette et al. 2015, v.4.2).

Once a 1D spectrum is obtained for each arm (combining together the different scientific exposures), we measure the redshift and the SNR of each galaxy independently from the three arms, using the entire spectral coverage.[5] Then, we convolve all of them to the same final resolution [full width at half-maximum ($\mathrm{FWHM_{fin}} = 2.51$ Å), at rest frame] and join them together, producing the final spectrum that we use to compute the stellar velocity dispersion and stellar population parameters, via full spectrum fitting, using stellar templates with the same FWHM.

Both single-arm spectra and the combined and smoothed ones are publicly released as part of the `INSPIRE` ESO Phase 3 collection.[6] A detailed description of how the arms have been joined together and how the data have been smoothed at the final resolution is provided in the data release description, while the final UVB + VIS smoothed spectra are shown in Appendix C.

---

[2] The source code of the package is available on request to the authors.

[3] In the particular case of J1026+0033, a second galaxy can be seen in the field of view. However, we stress that this object does not fit into the X-Shooter slit and hence does not influence the results presented in this paper.

[4] http://www.eso.org/sci/software/pipelines/skytools/molecfit

[5] We use the IDL code DER_SNR (Stoehr et al. 2008, https://www.stecf.org/software/ASTROsoft/DER_SNR) which estimates the SNR directly from the flux, assuming that the noise is uncorrelated in wavelength bins spaced two pixels apart and that it is approximately Gaussian distributed.

[6] https://archive.eso.org/scienceportal/home?data_collection = INSPIRE

Table 1. Morpho-photometric characteristics of the INSPIRE final sample. Magnitudes (*gri* in the AB system), median effective radii (R$_e$) in arcseconds and kpc, median Sérsic indices (*n*), median axis ratios (*q*), and stellar masses have all been inferred from KiDS images.

ID KiDS	RA (deg)	Dec. (deg)	DR	Sample	mag$_g$ (AB)	mag$_r$ (AB)	mag$_i$ (AB)	⟨R$_e$⟩ (″)	⟨R$_e$⟩ (kpc)	⟨n⟩	⟨q⟩	M$_\star$ (10^{11}M$_\odot$)
J0211−3155	32.8962202	−31.9279437	1	T18	21.28	19.78	19.28	0.24	1.07	8.10	0.48	0.88
J0224−3143	36.0902655	−31.7244923	1	T18	20.91	19.25	18.62	0.29	1.55	6.06	0.39	2.71
J0226−3158	36.5109217	−31.9810149	1	T18	20.63	19.25	18.76	0.35	1.32	3.65	0.60	0.69
J0240−3141	40.0080971	−31.6950406	1	T18	20.58	19.05	18.59	0.19	0.81	8.10	0.27	0.98
J0314−3215	48.5942558	−32.2632678	1	T18	21.00	19.57	19.07	0.15	0.66	5.54	0.39	1.00
J0316−2953	49.1896388	−29.8835868	1	T18	21.19	19.66	19.13	0.20	1.02	3.52	0.31	0.87
J0317−2957	49.4141028	−29.9561748	1	T18	20.51	19.10	18.63	0.26	1.05	5.01	0.21	0.87
J0321−3213	50.2954390	−32.2221290	1	T18	20.67	19.23	18.74	0.31	1.37	4.93	0.39	1.23
J0326−3303	51.5140585	−33.0540443	1	T18	20.94	19.48	18.99	0.32	1.43	3.66	0.35	0.93
J0838+0052	129.5304520	0.8823841	1	S20	20.65	19.29	18.75	0.31	1.28	4.02	0.41	0.87
J0842+0059	130.6665506	0.9899186	1	S20	21.12	19.60	19.06	0.23	1.01	3.27	0.29	0.91
J0844+0148	131.0553886	1.8132204	2	S20	21.25	19.78	19.26	0.26	1.14	6.56	0.49	0.71
J0847+0112	131.9112386	1.2057129	1	SDSS-GAMA	19.67	18.41	17.98	0.46	1.37	3.33	0.27	0.99
J0857−0108	134.2512185	−1.1457077	1	S20	20.72	19.21	18.70	0.34	1.40	2.94	0.33	1.00
J0904−0018	136.0518949	−0.3054848	2	S20	20.59	19.11	18.64	0.26	1.16	4.82	0.32	1.30
J0909+0147	137.3989150	1.7880025	2	SDSS-GAMA	20.06	18.68	18.16	0.30	1.05	9.97	0.77	1.05
J0917−0123	139.2701850	−1.3887918	2	S20	20.86	19.21	18.66	0.27	1.37	3.05	0.41	2.19
J0918+0122	139.6446428	1.3794780	1	T18	20.67	19.13	18.57	0.33	1.71	6.06	0.51	2.26
J0920+0126	140.1291393	1.4431610	2	S20	20.97	19.52	19.05	0.33	1.51	6.92	0.68	0.98
J0920+0212	140.2320835	2.2126831	1	SDSS-GAMA	20.35	18.87	18.43	0.34	1.48	1.99	0.32	1.03
J1026+0033	156.7231818	0.5580980	2	SDSS-GAMA	18.45	17.39	16.97	0.34	1.02	3.18	0.29	1.48
J1040+0056	160.2152308	0.9407580	2	S20	20.95	19.52	18.49	0.31	1.29	4.57	0.36	0.93
J1114+0039	168.6994335	0.6510299	2	S20	20.45	19.00	18.55	0.34	1.52	4.93	0.25	1.62
J1128−0153	172.0885023	−1.8890642	2	T18	19.87	18.56	18.07	0.35	1.27	6.69	0.31	1.30
J1142+0012	175.7023296	0.2043419	2	SDSS-GAMA	17.80	17.02	16.57	0.71	1.40	3.60	0.23	0.84
J1154−0016	178.6922829	−0.2779248	2	T18	20.90	19.52	18.73	0.22	1.06	4.36	0.19	0.64
J1156−0023	179.2186145	−0.3946596	2	SDSS-GAMA	20.06	18.83	18.08	0.26	1.04	6.53	0.38	1.39
J1202+0251	180.5132277	2.8515451	2	S20	20.97	19.43	18.96	0.31	1.49	6.47	0.89	0.68
J1218+0232	184.7355807	2.5449139	2	S20	20.78	19.23	18.71	0.31	1.40	2.75	0.26	0.93
J1228−0153	187.0640987	−1.8989049	2	S20	20.27	18.85	18.37	0.36	1.61	2.87	0.54	1.15
J1402+0117	210.7400749	1.2917747	3	S20	21.34	19.96	19.44	0.17	0.68	6.43	0.46	0.66
J1411+0233	212.8336012	2.5618381	2	S20	20.49	18.86	18.41	0.21	1.07	2.83	0.30	1.55
J1412−0020	213.0038281	−0.3440699	3	SDSS-GAMA	20.74	19.19	18.67	0.33	1.42	6.13	0.39	1.20
J1414+0004	213.5646898	0.0809744	3	SDSS-GAMA	20.41	18.99	18.50	0.31	1.42	4.26	0.42	1.18
J1417+0106	214.3685124	1.1073909	3	SDSS-GAMA	18.97	17.90	17.51	0.49	1.48	3.92	0.33	0.91
J1420−0035	215.1715599	−0.5864629	3	SDSS-GAMA	20.30	18.95	18.45	0.34	1.35	5.67	0.62	0.99
J1436+0007	219.0481314	0.1217459	2	SDSS-GAMA	19.55	18.27	17.85	0.39	1.40	2.65	0.19	1.15
J1438−0127	219.5218882	−1.4582727	3	SDSS-GAMA	20.65	19.29	18.74	0.28	1.20	4.11	0.38	0.88
J1447−0149	221.9657402	−1.8242806	3	SDSS-GAMA	19.86	18.61	18.16	0.44	1.51	3.06	0.45	0.86
J1449−0138	222.3504660	−1.6459975	3	SDSS-GAMA	20.86	19.40	18.92	0.35	1.44	5.81	0.33	1.03
J1456+0020	224.2361596	0.3353906	3	S20	20.88	19.46	18.97	0.12	0.50	5.53	0.20	0.71
J1457−0140	224.3397592	−1.6691725	3	S20	20.99	19.43	18.93	0.34	1.66	4.60	0.53	1.51
J1527−0012	231.7772381	−0.2065670	3	S20	21.37	19.67	19.08	0.23	1.26	5.77	0.23	1.74
J1527−0023	231.7522351	−0.3997483	3	S20	21.21	19.64	19.14	0.22	1.12	9.16	0.75	1.15
J2202−3101	330.5472803	−31.018381	2	T18	20.93	19.43	18.93	0.31	1.45	4.24	0.39	1.10
J2204−3112	331.2228147	−31.200261	2	SDSS-GAMA	20.84	19.32	18.86	0.35	1.39	6.36	0.31	0.90
J2257−3306	344.3966471	−33.114445	2	T18	20.80	19.42	18.95	0.29	1.18	4.31	0.41	0.93
J2305−3436	346.3356634	−34.603091	1	T18	21.26	19.69	19.12	0.31	1.29	3.89	0.40	0.86
J2312−3438	348.2389042	−34.648591	1	T18	20.90	19.32	18.79	0.24	1.25	2.25	0.43	1.34
J2327−3312	351.9910156	−33.200760	1	T18	20.99	19.35	18.80	0.28	1.51	5.94	0.67	1.57
J2356−3332	359.1261248	−33.533475	2	T18	21.31	19.81	19.27	0.22	1.06	4.28	0.34	0.98
J2359−3320	359.9851685	−33.333583	1	T18	21.11	19.59	19.05	0.24	1.04	4.49	0.39	1.07

We stress that, although spectra covering the entire XSH wavelength range (from the UVB to the NIR) are obtained and made available to the astronomical community, for the moment we limit our analysis and base our results only on the UVB + VIS. This is mainly because the single stellar population (SSP) modelling is much better understood in this wavelength range, while more investigation is needed in the NIR, especially regarding carbon-sensitive indices which are systematically underestimated by the current SSP models (Eftekhari et al. 2022).

We rederive stellar velocity dispersion values ($\sigma_\star$) for all the `INSPIRE` objects, using the same parameters in the Penalized Pixel-

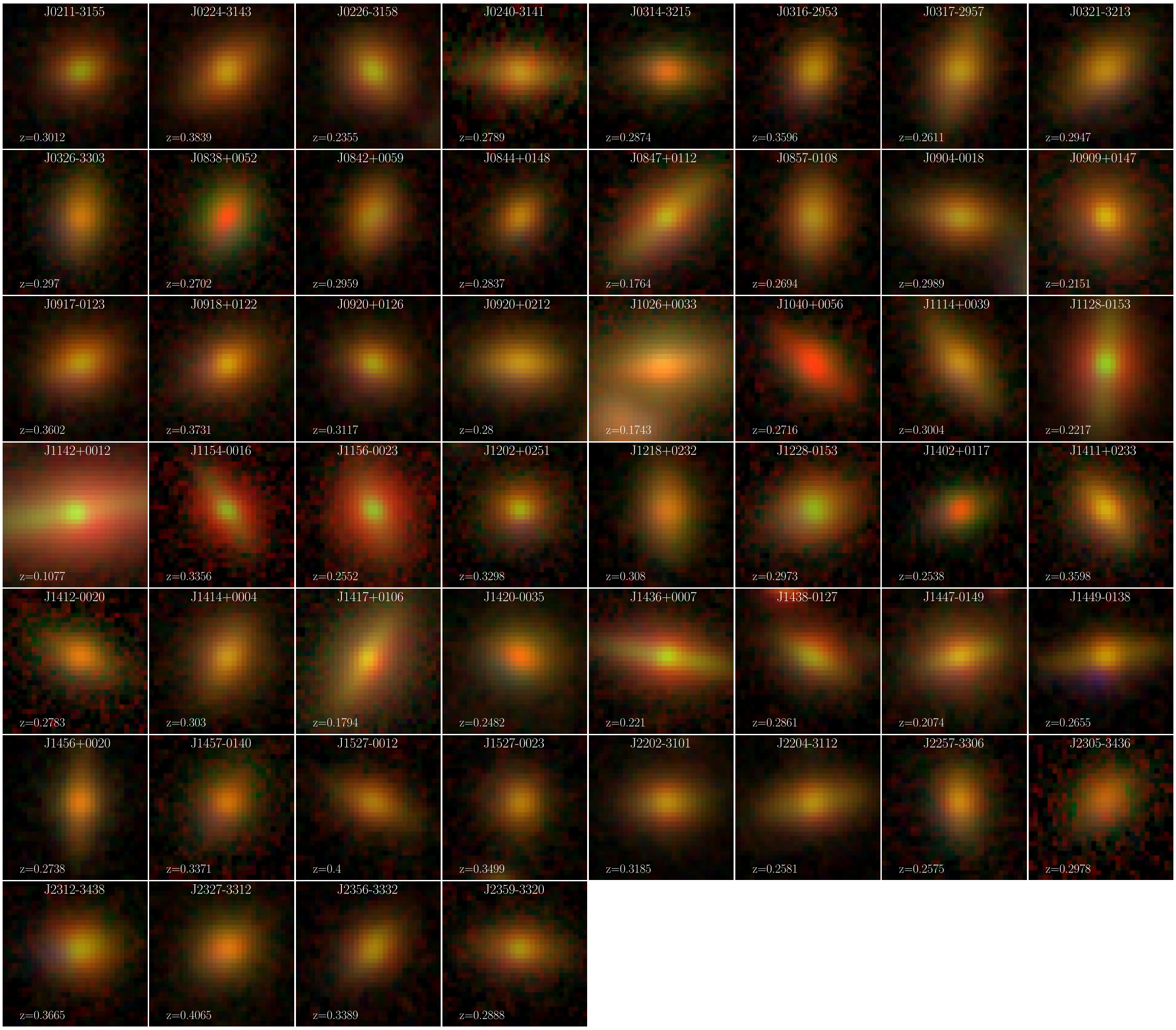

Figure 1. Colour-composite *gri* KiDS images of the 52 INSPIRE galaxies. Each panel has dimension of 6 arcsec × 6 arcsec and shows the ID of the corresponding galaxy on the top and its redshift on the bottom-left corner. For more details on astrometry and centring, see the text (Section 2.2).

fitting software[7] (PPXF; Cappellari & Emsellem 2004; Cappellari 2017) for each of the galaxies. We fix the wavelength range of the fit to [3500–9000] Å, and the additive Legendre polynomial degree (DEGREE) to 13. We use the keyword CLEAN to perform a sigma-clipping on the spectra and clean them from residual bad pixels. As stellar library for the fit, we use the E-MILES SSP models (Vazdekis et al. 2016). These models are an extention of the MILES models (Sánchez-Blázquez, Gorgas & Cardiel 2006; Vazdekis et al. 2015), covering the spectral range [1680–50 000] Å and have a spectral resolution of FWHM∼2.5 Å in the wavelenght range used for the fit.

In INSPIRE DR2 we have performed a comprehensive series of tests to assess the uncertainties on the velocity dispersion measurements arising from changing the fitted region, the mask for bad pixels, the degree of the additive polynomial, the resolution and SNR of the input spectrum, and the number of moments of the line-of-sight velocity distribution fitted by the routine. By means of a bootstrapping procedure realized ad hoc for the purpose, we showed that the uncertainties on $\sigma_\star$ are of the order of 10–15 per cent for the lowest SNR spectra (∼20 per Å) and ∼5 per cent for the highest SNR ones (∼80 per Å), as visible from fig. 6 in the INSPIRE DR2. Hence, we split the 52 UCMGs into three groups and assign a different uncertainty ($\Delta\sigma_\star$) to them. The low SNR group, with a relative error of 15 per cent on the velocity dispersion, comprises spectra with mean SNR ranging from 15 to 25. The objects in the medium SNR group, with spectra with mean SNR from 25 to 35, have an uncertainty on the stellar velocity dispersion of 10 per cent, while objects in the high SNR group (>35) have an uncertainty of 5 per cent.

Table 2 presents the characteristics of the INSPIRE sample that have been estimated from the 1D spectra directly. The typical

---

[7] https://pypi.org/project/ppxf/

Table 2. Spectroscopic properties of the `INSPIRE` sample: redshift, SNR in the three arms and their mean, and velocity dispersion obtained from the smoothed and combined 1D spectrum. Galaxies are listed in descending order of mean SNR per Å and split into three groups, as described in the text.

ID KiDS	z	SNR UVB	SNR VIS	SNR NIR	SNR mean	$\sigma_\star$ (km s^{-1})
J1142+0012	0.1077	57.9	124.1	58.2	80.0	129 ± 6
J1026+0033	0.1743	38.9	113.6	56.9	69.8	225 ± 11
J1417+0106	0.1794	39.9	107.7	26.6	58.1	203 ± 10
J2312−3438	0.3665	32.1	72.4	33.6	46.1	221 ± 11
J0909+0147	0.2151	20.7	75.3	37.6	44.5	401 ± 20
J0847+0112	0.1764	24.6	77.5	31.2	44.4	244 ± 12
J0224−3143	0.3839	20.9	71.2	36.3	42.8	283 ± 14
J1228−0153	0.2973	23.2	70.1	34.0	42.4	191 ± 10
J1128−0153	0.2217	21.1	69.2	30.8	40.4	192 ± 10
J1411+0233	0.3598	24.1	73.2	22.4	39.9	217 ± 11
J0838+0052	0.2702	22.6	65.2	31.8	39.9	189 ± 9
J0918+0122	0.3731	17.6	70.2	31.6	39.8	242 ± 12
J2327−3312	0.4065	19.6	72.8	25.8	39.4	227 ± 11
J0321−3213	0.2947	21.9	66.4	26.7	38.3	211 ± 11
J1436+0007	0.2210	21.1	67.2	24.2	37.5	193 ± 19
J1447−0149	0.2074	24.7	64.7	22.1	37.2	187 ± 9
J1156−0023	0.2552	22.6	60.9	26.5	36.7	177 ± 18
J0314−3215	0.2874	20.7	54.6	31.2	35.5	178 ± 9
J0326−3303	0.2970	21.4	54.5	26.7	34.2	173 ± 17
J0226−3158	0.2355	22.9	58.7	20.5	34.0	185 ± 19
J0240−3141	0.2789	17.9	54.5	26.9	33.1	216 ± 22
J0920+0126	0.3117	17.9	55.6	24.7	32.7	190 ± 19
J1438−0127	0.2861	17.9	59.4	20.2	32.5	218 ± 22
J1114+0039	0.3004	19.5	54.0	23.7	32.4	181 ± 18
J0920+0212	0.2800	17.0	55.0	21.9	31.3	246 ± 25
J2204−3112	0.2581	14.4	54.1	20.4	29.6	227 ± 23
J0317−2957	0.2611	20.1	51.7	15.5	29.1	187 ± 19
J2359−3320	0.2888	15.6	49.1	21.2	28.6	267 ± 27
J0917−0123	0.3602	12.2	50.3	22.9	28.5	239 ± 24
J0316−2953	0.3596	14.3	46.4	24.4	28.3	192 ± 19
J1040+0056	0.2716	11.5	46.7	26.2	28.1	240 ± 24
J2305−3436	0.2978	14.3	46.8	21.1	27.4	295 ± 30
J0211−3155	0.3012	13.9	46.7	21.4	27.3	245 ± 25
J1202+0251	0.3298	14.7	45.9	21.1	27.3	165 ± 17
J0844+0148	0.2837	12.9	45.0	23.3	27.1	224 ± 22
J0842+0059	0.2959	12.4	41.5	25.5	26.5	324 ± 32
J1154−0016	0.3356	16.6	42.8	19.6	26.3	163 ± 16
J0904−0018	0.2989	12.6	44.3	21.4	26.1	205 ± 21
J2257−3306	0.2575	17.8	40.0	20.0	25.9	185 ± 19
J2202−3101	0.3185	13.1	47.6	17.0	25.9	221 ± 22
J0857−0108	0.2694	15.7	43.3	18.6	25.8	166 ± 17
J1218+0232	0.3080	14.6	42.0	18.9	25.2	171 ± 17
J1420−0035	0.2482	13.4	39.8	15.5	22.9	209 ± 31
J1449−0138	0.2655	10.2	40.3	15.9	22.1	192 ± 29
J1456+0020	0.2738	11.9	39.6	14.4	22.0	194 ± 29
J1414+0004	0.3030	11.7	37.4	15.3	21.5	205 ± 31
J2356−3332	0.3389	11.5	34.2	14.8	20.1	162 ± 24
J1457−0140	0.3371	12.5	34.1	12.4	19.7	203 ± 30
J1402+0117	0.2538	12.4	34.0	11.9	19.5	166 ± 25
J1412−0020	0.2783	10.5	31.1	14.2	18.6	339 ± 51
J1527−0012	0.4000	7.1	32.7	14.6	18.1	237 ± 36
J1527−0023	0.3499	9.0	30.4	13.5	17.7	188 ± 28

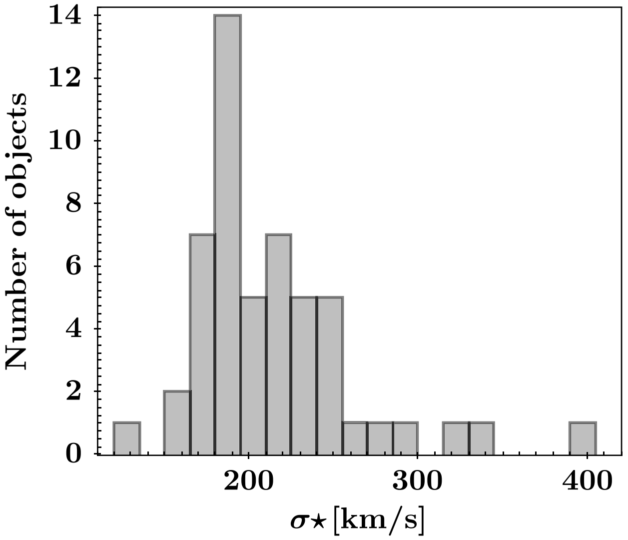

Figure 2. Distribution of the stellar velocity dispersion measurements for the entire INSPIRE sample.

uncertainties on the redshift are of the order of 0.1–0.5 per cent. The last column of the table reports the stellar velocity dispersion values obtained via full spectral fitting, as described above, and the associated uncertainties. The objects are ordered from the highest to the lowest mean SNR, and the three groups are separated by a horizontal line. We note that we take the arithmetic mean of the SNRs computed from each single arm (listed in the table), using all the pixels, to split the systems into the groups.

Fig. 2 shows the distribution of $\sigma_\star$ for the final INSPIRE sample. As expected from the range in stellar masses covered by the galaxies, the peak in velocity dispersion is ∼215 km s^{-1}, with however a long tail towards larger velocity dispersion values. In Section 5, we will show that this tail correlates with the DoR of the objects, as already hinted in `INSPIRE` DR1: galaxies with a higher DoR have overall larger stellar velocity dispersion with respect to galaxies of equal stellar mass but lower DoR.

4 STELLAR POPULATIONS ANALYSIS

Following the steps of previous `INSPIRE` papers, we use line-indices to derive the [Mg/Fe] abundance for each UCMG, and then the PPXF; (Cappellari & Emsellem 2004; Cappellari 2017) to perform a full spectral fit of the UCMGs spectra, computing integrated, mass-weighted ages, and metallicities. The two processes are described in the next sections.

For both the line-indices and the full-spectral fitting, we use the MILES models described in Vazdekis et al. (2015) with BaSTI theoretical isochrones[8] (Pietrinferni et al. 2004, 2006). These models allow the user to investigate a broad range of stellar ages from 30 Myr to 14.5 Gyr (sampled at logarithmic steps), metallicities in the range −1.79 <[M/H]<+0.40 and a suite of stellar IMF slopes. The fitted range for the PPXF stellar population analysis is [3525–7500] Å, which corresponds to entire range covered by the SSP libraries.

---

[8] http://www.oa-teramo.inaf.it/BASTI.

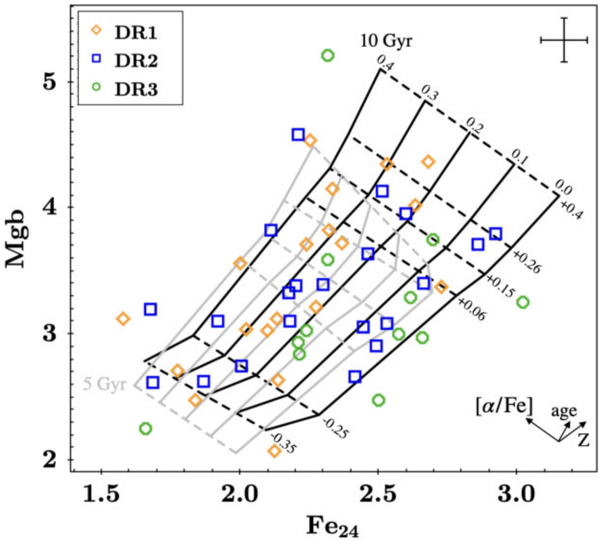

Figure 3. Mg$_b$-Fe24 index–index plot used to infer the [Mg/Fe] for all the INSPIRE objects. The grid shows MILES SSPs with two different ages (10 Gyr in black and 5 Gyr in grey), covering a range of metallicities and [α/Fe] values. The direction of variation for age, metallicity, and [α/Fe] is given by the arrows in the bottom-right corner. The [α/Fe] is orthogonal to the other parameters and hence can be inferred even without a precise estimate of age and metallicity. The `INSPIRE` galaxies are colour-coded and have different symbols, according to the Data Release to which they belong to. A typical error-bar is shown on the right-top corner of the plot.

4.1 SSP-equivalent [Mg/Fe] abundances from line-indices

The [Mg/Fe] abundance is often used as a proxy for the time-scale efficiency of the SF episode. For a fixed IMF, a large [Mg/Fe] value indicates a very quick quenching of SF, which occurs before Type Ia supernova explosions can pollute the interstellar medium with iron (e.g. Matteucci 1994; Thomas et al. 2005; Gallazzi et al. 2006, 2021). Hence, since relics should have formed the (almost) totality of their stellar mass in a very fast SF burst, they are expected to have a very large [Mg/Fe] abundance. Indeed, a high, supersolar ratio has been measured for the three local relics (Ferré-Mateu et al. 2017; Yıldırım et al. 2017; Martín-Navarro et al. 2018) and for the confirmed relics in `INSPIRE` DR1.

Since measuring [α/Fe] from full-spectral fitting requires further tests (see e.g. Vazdekis et al. 2015 and Liu 2020), we estimate the [Mg/Fe] via the analysis of line-index strengths from Mg and Fe lines. To reproduce exactly what has been done in `INSPIRE` DR1, we use the Mg$_b$ (5177 Å) and the mean of 24 different iron lines present in the spectral range [3500–7000] Å. Combining many different Fe-lines helps to minimize the dependency on other elemental abundances (e.g. [Ti/Fe]) which might fall in the Fe-indices bandpasses. We have however tested our result against a different combination of Fe-lines, finding results overall consistent within the uncertainties.

We use the code SPINDEX from Trager, Faber & Dressler (2008) to calculate the strengths of these features from the galaxies' spectra, all convolved to a common velocity dispersion of 402 km s^{-1}, equal to the maximum stellar velocity dispersion (the same of J0909+0147). We then measure the line-index strengths of the same spectral features in SSP models brought to the same resolution. We use two sets of ages (5 and 10 Gyr, justified by the results of DR1), metallicities ranging from −0.35 to +0.4, and a bimodal IMF with $\Gamma = 1.3$ (resembling a Kroupa IMF). We note that the MILES models do not allow to control the [Mg/Fe] directly, but this can be approximated to [α/Fe], which is the parameter we can change in the SSPs. The version of the MILES models we employ here is available only at two different [α/Fe] abundances: 0.0 (solar) and 0.4. We note that a new version of the MILES models has very recently been released (Knowles et al. 2023). These models allow for variation in [α/Fe] from −0.2 to +0.6 with steps of 0.2. However, as pointed out by the authors of the SSP models, for [α/Fe] enhancements from scaled-solar to 0.4, the abundance pattern predictions from the new models and that obtained from the old ones show only minimal differences for old SSP ages over a wide range of total metallicities.

The result of the line-indices analysis can be visualized via the Mg$_b$-Fe$_{24}$ index–index plot, shown in Fig. 3. In this plot, age and metallicity are degenerate, both increasing from the bottom-left corner to the top right one. The [α/Fe] varies instead in an orthogonal direction, as shown by the arrows in the bottom-right corner of the figure. Therefore, this particular pair of indices allows us to estimate the [Mg/Fe] for all the UCMGs, even before having a precise constraint on the age and metallicity. In order to build a finer grid, we linearly interpolate the models (0.0 and 0.4 in [α/Fe]) in steps of Δ[α/Fe] = 0.1. We prefer not to extrapolate the models outside the original boundaries. We then directly estimate the [Mg/Fe] from the plot, taking as value the [α/Fe] of the closest model to each point on the 10 Gyr grid. Given that there is no prior on age and metallicity and these will slightly shift the model grids, we assign an uncertainly of 0.1 to all the [Mg/Fe] values, which is equal to the step between the models. We could have computed a more precise estimate of the [Mg/Fe] by interpolating the models over a fine grid, also in age and metallicity. However we decided not to do so since these 'SSP-equivalent' [Mg/Fe] estimates, which are listed in the second column of Table 3, will only be used to select SSP models with a given [α/Fe] as input in the full-spectral fitting, as detailed in Section 4.2. We note that for six DR1 systems we find an estimate that deviated by ±0.1 from that estimated in `INSPIRE` DR1. This might be due to small differences in the line-indices measurements that could be caused by the different smoothing applied here.[9]

4.2 Mass-weighted stellar ages and metallicities from full-spectral fitting

Mass-weighted stellar ages and metallicities are obtained with PPXF performing a full-spectral fitting on the integrated 1D R50 spectra. Also in this case, for consistency, we use the MILES single SSP models as stellar templates for the fit. For our purposes, we use models with ages from 1 Gyr to the age of the Universe at the redshift of each object[10] (logarithmic sampled with steps of $\Delta \log t$ = 0.5 Gyr). In future `INSPIRE` publications, we will extend the analysis to the UVB arm (at wavelengths bluer than 3500 Å) in order to increase the sensitivity to younger ages. This is motivated by the finding of Salvador-Rusiñol et al. (2021) and Salvador-Rusiñol et al. (2022), which detected residual sub-one per cent recent SF in massive ETGs and in the local relic NGC1277.

---

[9] In DR1 the largest velocity dispersion value was $\sigma = 300$ km s^{-1}, and hence both galaxies and SSP were convolved to that resolution.

[10] Given the sampling of the SSPs in age ($\Delta_{\rm age} = 0.5$ Gyr), we allow models up to 0.5 older than the age of the Universe at the galaxies' redshifts.

Table 3. Results of the stellar population analysis. The first block of columns after the ID lists the 'SSP-equivalent' [Mg/Fe] abundances, and the mass-weighted ages and metallicities in the unregularized case (unr) and using the maximum regularization allowed by the data (rmax). Uncertainties are obtained via bootstrapping. In the third block of columns, we list the minimum fraction of stellar mass assembled by $z = 2$, the cosmic time at which the galaxies had formed 75 per cent of their mass, the cosmic time of final assembly, and the age of the Universe at the redshift of the galaxies. Galaxies are ordered from the highest (most extreme relic) to the lowest (extended SFH) DoR, which are listed in the last column and the horizontal line separates the extreme relics.

ID KiDS	[Mg/Fe] (±0.1 dex)	$t_{\rm unr}$ (Gyr)	$t_{\rm rmax}$ (Gyr)	Δt (Gyr)	$[M/H]_{\rm unr}$ dex	$[M/H]_{\rm rmax}$ dex	$\Delta[M/H]$ dex	$f_{M^{\star}_{t_{\rm BB}=3}}$	t_{75} (Gyr)	$t_{\rm fin}$ (Gyr)	$t_{\rm Uni,\,z}$ (Gyr)	DoR
J0847+0112	0.3	12.0	11.6	0.2	0.30	0.35	0.02	0.9988 ± 0.0002	0.9 ± 0.3	2.0 ± 0.7	11.52	0.83
J2305−3436	0.3*	10.5	10.1	0.2	0.32	0.34	0.02	0.9980 ± 0.0007	1.0 ± 0.3	2.0 ± 0.7	10.29	0.80
J0909+0147	0.4	11.4	11.1	0.3	0.27	0.31	0.02	0.9950 ± 0.0013	0.9 ± 0.2	3.0 ± 4.0	11.11	0.79
J2204−3112	0.3	11.0	10.6	0.3	0.27	0.30	0.02	0.9992 ± 0.0003	1.0 ± 0.4	2.5 ± 0.9	10.67	0.78
J1438−0127	0.4	10.5	10.1	0.4	0.05	0.11	0.05	0.9971 ± 0.0013	0.9 ± 0.3	3.0 ± 1.1	10.40	0.78
J1040+0056	0.4	10.9	10.6	0.3	0.27	0.28	0.02	0.991 ± 0.003	1.0 ± 0.3	3.0 ± 3.9	10.54	0.77
J0842+0059	0.4	10.5	10.0	0.2	0.22	0.26	0.02	0.983 ± 0.007	1.1 ± 0.3	3.5 ± 1.8	10.31	0.73
J0211−3155	0.3	10.4	9.9	0.2	0.26	0.28	0.03	0.989 ± 0.003	1.1 ± 0.3	3.5 ± 4.0	10.26	0.72
J2359−3320	0.2	10.4	9.7	0.2	0.34	0.33	0.03	0.993 ± 0.002	1.4 ± 0.4	3.0 ± 3.9	10.38	0.71
J0920+0212	0.3	10.4	9.9	0.3	0.23	0.26	0.03	0.968 ± 0.012	0.9 ± 0.2	7.0 ± 3.8	10.46	0.64
J1412−0020	0.0	10.3	9.3	0.3	0.40	0.32	0.03	0.93 ± 0.03	1.9 ± 0.6	4.5 ± 4.1	10.48	0.61
J1449−0138	0.3	10.9	10.2	0.3	0.21	0.25	0.03	0.961 ± 0.016	1.3 ± 0.3	6.5 ± 3.8	10.60	0.60
J0224−3143	0.3	9.8	9.4	0.3	0.18	0.21	0.03	0.976 ± 0.004	0.9 ± 0.2	9.0 ± 3.7	9.53	0.56
J0838+0052	0.3*	10.5	9.8	0.5	0.11	0.13	0.04	0.85 ± 0.05	1.9 ± 0.6	6.0 ± 3.3	10.56	0.54
J0317−2957	0.4	10.6	10.3	0.3	0.17	0.19	0.04	0.949 ± 0.018	1.1 ± 0.3	10.0 ± 4.0	10.64	0.51
J2202−3101	0.2	10.4	9.5	0.5	0.18	0.22	0.03	0.82 ± 0.07	1.5 ± 0.4	8.0 ± 2.9	10.10	0.48
J1457−0140	0.2	9.2	8.5	0.5	0.11	0.12	0.05	0.81 ± 0.07	2.1 ± 0.7	7.0 ± 2.7	9.93	0.47
J0844+0148	0.4	9.8	9.1	0.1	0.12	0.17	0.05	0.91 ± 0.03	1.5 ± 0.4	10.0 ± 4.0	10.43	0.45
J1218+0232	0.3	10.2	9.3	0.4	0.06	0.14	0.05	0.89 ± 0.04	1.5 ± 0.5	9.5 ± 3.3	10.20	0.45
J2356−3332	0.2	8.9	7.9	0.7	0.25	0.29	0.05	0.90 ± 0.02	1.7 ± 0.6	9.5 ± 3.9	9.92	0.44
J0917−0123	0.4	9.6	8.4	0.3	0.10	0.18	0.04	0.89 ± 0.04	1.6 ± 0.5	9.5 ± 3.9	9.73	0.44
J0918+0122	0.2*	9.3	8.6	0.3	0.20	0.23	0.05	0.90 ± 0.03	1.6 ± 0.5	9.5 ± 4.0	9.62	0.43
J0240−3141	0.0	9.1	8.5	0.7	0.29	0.29	0.02	0.90 ± 0.03	1.9 ± 0.6	10.0 ± 3.9	10.47	0.43
J0314−3215	0.2*	9.0	8.1	0.5	0.22	0.26	0.05	0.87 ± 0.02	1.8 ± 0.6	10.0 ± 4.1	10.39	0.42
J1420−0035	0.1	10.5	9.2	0.5	0.29	0.30	0.03	0.87 ± 0.05	2.2 ± 0.8	10.0 ± 3.9	10.77	0.41
J1411+0233	0.2	8.5	7.8	0.5	0.15	0.18	0.04	0.84 ± 0.04	1.7 ± 0.5	9.5 ± 4.1	9.74	0.41
J1114+0039	0.2	9.2	8.2	0.5	0.21	0.25	0.03	0.86 ± 0.04	1.9 ± 0.6	10.0 ± 3.6	10.27	0.40
J0316−2953	0.4*	9.1	8.0	0.3	−0.10	0.02	0.08	0.83 ± 0.06	1.9 ± 0.5	9.5 ± 4.1	9.74	0.40
J1228−0153	0.3	10.1	9.0	0.6	0.05	0.09	0.05	0.82 ± 0.08	2.3 ± 0.7	9.5 ± 3.8	10.3	0.39
J0857−0108	0.2	10.1	9.1	0.4	0.21	0.21	0.04	0.80 ± 0.05	2.6 ± 0.9	9.5 ± 4.0	10.56	0.39
J1447−0149	0.1	10.9	9.8	0.7	0.13	0.18	0.04	0.82 ± 0.07	2.5 ± 0.9	10.5 ± 4.3	11.19	0.38
J1527−0012	0.2	8.7	7.7	0.6	0.124	0.18	0.05	0.79 ± 0.05	2.7 ± 0.9	8.5 ± 3.2	9.4	0.38
J1527−0023	0.2	8.4	7.4	0.9	0.11	0.12	0.09	0.81 ± 0.06	2.4 ± 0.8	9.5 ± 3.4	9.82	0.37
J0321−3213	0.4	8.8	8.7	0.4	0.06	0.04	0.05	0.81 ± 0.06	2.4 ± 0.7	10.0 ± 3.7	10.32	0.37
J2312−3438	0.3	9.0	8.6	0.4	0.012	0.03	0.04	0.80 ± 0.07	2.5 ± 0.7	9.5 ± 3.9	9.68	0.36
J1414+0004	0.2	9.9	8.4	0.5	0.07	0.14	0.06	0.80 ± 0.08	2.5 ± 0.9	10.0 ± 4.1	10.24	0.36
J1202+0251	0.2	8.5	7.3	0.7	0.18	0.18	0.06	0.78 ± 0.06	2.6 ± 0.9	9.5 ± 3.1	10.0	0.36
J1128−0153	0.0	10.3	9.4	0.5	0.26	0.25	0.02	0.75 ± 0.09	2.9 ± 1.1	10.5 ± 4.3	11.04	0.34
J1436+0007	0.1	10.0	8.4	0.8	0.25	0.27	0.03	0.72 ± 0.09	3.1 ± 1.1	10.5 ± 4.4	11.05	0.33
J1417+0106	0.0	8.6	8.0	0.6	0.19	0.18	0.03	0.72 ± 0.08	3.6 ± 1.2	10.5 ± 3.6	11.49	0.33
J0904−0018	0.1	8.6	7.8	0.5	0.36	0.28	0.04	0.70 ± 0.10	3.2 ± 1.1	10.0 ± 3.8	10.28	0.32
J1402+0117	0.0	9.0	8.5	0.9	0.17	0.17	0.05	0.70 ± 0.07	3.2 ± 1.1	10.5 ± 4.1	10.72	0.31
J1156−0023	0.0	7.3	6.7	0.8	0.20	0.20	0.03	0.69 ± 0.06	3.6 ± 1.2	10.5 ± 4.1	10.7	0.30
J1026+0033	0.3	9.9	9.3	0.4	0.03	0.03	0.03	0.67 ± 0.05	3.6 ± 1.5	11.5 ± 3.2	11.55	0.29
J2257−3306	0.1	8.3	8.5	0.7	0.20	0.21	0.03	0.63 ± 0.12	8.1 ± 3.1	10.0 ± 4.2	10.68	0.27
J0920+0126	0.1*	8.5	7.0	0.9	0.14	0.14	0.05	0.56 ± 0.13	8.5 ± 3.4	9.5 ± 3.9	10.16	0.25
J0326−3303	0.3	8.0	8.4	0.6	−0.08	−0.09	0.05	0.50 ± 0.17	3.3 ± 1.2	10.0 ± 3.5	10.3	0.25
J1142+0012	0.3	6.3	5.3	0.6	0.13	0.11	0.04	0.42 ± 0.12	11.5 ± 4.8	12.0 ± 3.3	12.32	0.18
J1456+0020	0.0	5.3	5.3	1.1	0.08	0.12	0.06	0.32 ± 0.09	8.7 ± 3.4	10.0 ± 2.1	10.52	0.17
J1154−0016	0.0	3.8	3.8	0.8	−0.05	−0.05	0.07	0.17 ± 0.14	8.3 ± 3.4	9.5 ± 3.3	9.95	0.11
J0226−3158	0.0	5.0	5.3	1.0	0.18	0.21	0.04	0.09 ± 0.30	7.1 ± 3.2	9.5 ± 2.5	10.9	0.12
J2327−3312	0.2	2.7	2.7	0.5	0.17	0.16	0.04	0.00 ± 0.18	8.4 ± 3.5	9.0 ± 0.4	9.34	0.06

Note. *For these systems the new estimate is 0.1× higher/lower than that of DR1.

The PPXF fit is performed in 2D, only letting age and metallicity vary in the models. In fact, as already done in `INSPIRE` DR1, we use, for each galaxy, only models with the [α/Fe] ratio equal to that estimated from line-indices. In future `INSPIRE` publications, we will improve on this aspect by implementing a PPXF fit in 3D, or even 4D, also varying the IMF slope, which is kept fixed to a bimodal-distribution with a low-mass end slope of $\Gamma = 1.3$. In fact, the DR1 data hinted at a difference in the low-mass end of the IMF slope between relics and non-relics (Martín-Navarro et al. 2023); however, a much higher SNR is necessary to measure IMF variations and break the degeneracies with the other stellar population parameters (e.g. Conroy & van Dokkum 2012; La Barbera et al. 2013; Spiniello et al. 2014). We will investigate how a variable IMF might influence the other stellar population parameters and whether or not the slope correlates with the DoR in a forthcoming paper, stacking galaxies with similar DoR or other parameters.

Following `INSPIRE` DR1, we perform the PPXF fit using the two most extreme values of the regularization parameter, thus deriving the minimally (REGUL = 0, hereafter ‘unr’) and maximally smoothed (REGUL = MAX_REGUL, hereafter ‘rmax’) solutions consistent with each spectrum and its SNR. The MAX_REGUL changes from system to system and it is calculated by rescaling the noise until the χ^2 increases by $\Delta\chi^2 = \sqrt{2 \times \mathrm{DoF}}$, where the degree of freedom is approximated to be equal to the number of pixels used in the fit. Unlike for the kinematics, we only use multiplicative polynomials for the stellar populations to preserve the line strengths. We set the multiplicative polynomial degree MDEGREE = 10 (see the tests performed in appendix A of the `INSPIRE` Pilot). To estimate reliable uncertainties on the mass-weighted ages and metallicities, we run a bootstrap routine consisting in repeatedly fitting a PPXF model to a spectrum obtained by adding random noise to the original one. The random noise is within three times the RMS obtained by subtracting from the original spectrum a median smoothed version of itself. We repeat this procedure 256 times and use the standard deviation as uncertainty on the measured stellar population parameters. At this stage, we also vary the MDEGREE (within ±2) and the REGUL parameter (within MAX_REGUL−5 and MAX_REGUL).

Fig. 4 shows two examples of PPXF fits for the olderst (top) and the youngest (bottom) UCMGs. In the left panels, the galaxy spectrum is plotted in black, while the best-fitting SSP template is overplotted in red. The right panels show the mass and metallicity inferences from the weights of the SSP models, used to build the best fit, in the rmax case.

Results obtained in the two extreme PPXF configurations (unr and rmax) can be seen in the scatter plots of Fig. 5. In the top panel, we plot the formation epoch of each galaxy, defined as the difference between the age of the Universe at the redshift of each object and the stellar age derived from full spectral fitting ($t_{\mathrm{Uni,\,z}} - t_{\mathrm{gal}}$) for the unr case ($x$-axis) versus the rmax one (y-axis). This quantity is a proxy for the formation age of the systems: the closer this number is to zero, the earlier the object assembled its stellar mass in the history of the Universe. Smoother solutions clearly imply younger ages. Since in principle, regularized and unregularized solutions should be statistically equivalent, the fact that they produce mass-weighted mean ages that are only marginally consistent within the plotted error bars demonstrates that our bootstrapping routine produces uncertainties that only take into account the uncorrelated noise in the spectra but are not sensitive to systematics arising from the regularization of the fits.

The bottom scatter plot shows the different estimates of [M/H] in the two cases. As expected, younger ages (in the rmax case) translate into higher metallicities. However, since the difference between the two PPXF runs is small, the regularization does not play a major role in constraining the stellar metallicity. The histograms on the corners of each panels show the distribution of formation ages and metallicities for the two regularizations.

All stellar population results are summarized in Table 3, where we report the [Mg/Fe] values estimated from line-indices analysis and the mass-weighted ages and metallicities for the unr and the rmax cases. These quantities are used to compute SFHs, and in particular the fraction of stellar mass assembled in cosmic time. Specifically, this latter quantity is computed from the age-[M/H]’weights fractions maps’ (density maps) shown in the right panels of Fig. 4, by flipping the age axis and marginalizing over metallicity. This quantity will be used in the next section to estimate the DoR and assess how many of the `INSPIRE` UCMGs can be classified as relics of the ancient Universe.

5 RESULTS

In `INSPIRE` DR1 we have computed the fraction of mass assembled within 3 Gyr after the big bang ($f_{M^{\star}_{t\mathrm{BB}=3}}$), i.e. by $z = 2$, assumed to be the end of the first phase (Zolotov et al. 2015), the cosmic time at which 75 per cent of the stellar mass was in place (t_{75}), and the time of final assembly, i.e the cosmic time at which the entire totality (100 per cent) of the stellar mass was in place (t_{fin}). This allowed us to weigh the contribution by ancient stars separating them from those formed in later episodes of SF (if any) and how much they extended in cosmic time. Here, we compute the same quantities for all the 52 `INSPIRE` objects and list them in Table 3, alongside with the stellar population results.

To produce the stellar mass assembled in cosmic time, we start from the density maps, like the ones shown in the right panels of Fig. 4. We flip the age axis and sum over all metallicity values, computing in this way the fraction of mass assembled at each age bin since the big bang to the redshift of the galaxy. In `INSPIRE` DR1 we use the $f_{M^{\star}_{t\mathrm{BB}=3}}$ and t_{75} to classify UCMGs in relics and non-relics. In particular, the quantities we quote in the table are the minimum $f_{M^{\star}_{t\mathrm{BB}=3}}$ and the maximum t_{75} of the four different estimates obtained from four different PPXF configurations:

(i) an unregularized fit using models with [α/Fe] equals to the [Mg/Fe] value estimated from line-indices,

(ii) the fit using the maximum regularization and models with [α/Fe] = [Mg/Fe],

(iii) an unregularized fit using models with [α/Fe] = [Mg/Fe]+0.1,

(iv) an unregularized fit using models with [α/Fe] = [Mg/Fe]−0.1.

The uncertainty is assumed to be the standard deviation between the same four estimates.

The uncertainties we associate with $f_{M^{\star}_{t\mathrm{BB}=3}}$ and t_{75} are assumed to be the standard deviation on the four measurements. It is very interesting to note that high $f_{M^{\star}_{t\mathrm{BB}=3}}$ have much smaller uncertainties. This is because for extremely peaked SFHs, the PPXF configurations do not play a major role and the four estimates are very similar. This is not true for systems with a more time-extended SFH. Finally, the remaining two columns of the same block list instead the final assembly time (t_{fin}, 100 per cent of the mass formed) and the age of the Universe at the redshifts of the objects ($\mathrm{t}_{\mathrm{Uni,\,z}}$).

5.1 The DoR

In `INSPIRE` DR1, we used the minimum fraction (among those obtained from different PPXF set-ups) of stellar mass assembled at $z = 2$ and the maximum cosmic time at which 75 per cent of the

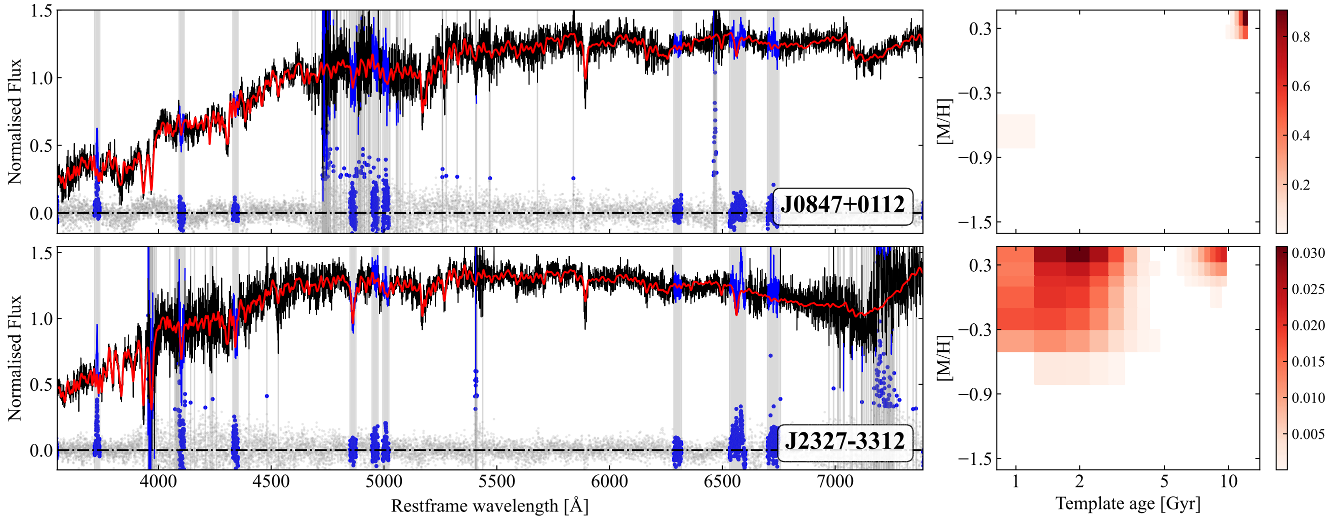

Figure 4. The pPXF fits for the oldest (top) and the youngest (bottom) galaxies. The left panels show the fits, with the galaxy spectrum in black, the SSP best-fitting template in red, residuals in grey, and pixels masked out from the fit in blue. The right panels show the age–metallicity density map obtained for the maximum regularized case. They represent the mass-weighted fraction assigned by pPXF to each input SSP.

stellar mass was in place to classify the 19 systems analysed there into three groups: extreme relics, relics, and non-relics. Here, we also consider the cosmic time of final assembly in order to resolve the diversity of the entire `INSPIRE` sample. We need to be able to disentangle between an object that had formed the majority of its stellar mass early on in cosmic time but then underwent a very time-extended SF from an object that assembled a similar quantity of stellar mass during the first burst, but then completed its formation still at high z.

In addition, this time, we combine these three quantities together defining a number for each object, hence expressing the relicness with a simple parameter that quantifies the mean SFH and that gives a sense of the diversity of galaxies in terms of their stellar populations. The DoR is defined as

$$\mathrm{DoR} = \left[f_{M^{\star}_{t\mathrm{BB}=3}} + \frac{0.5\mathrm{Gyr}}{t_{75}} + \frac{0.7\mathrm{Gyr} + (t_{\mathrm{Uni}} - t_{\mathrm{fin}})}{t_{\mathrm{Uni}}} \right] \times \frac{1}{3} \qquad (1)$$

The equation is motivated by the very recent findings of Labbé et al. (2023) that it takes about 500–700 Myr to form a galaxy with $M_{\star} \sim 10^{11}\mathrm{M}_{\odot}$. Hence, the minimum time to form 75 per cent of the stellar mass is set to 0.5 Gyr, while the minimum time to assemble all the mass is set to 0.7 Gyr. The third addendum is related to the final assembly time (i.e. the time at which a galaxy has formed the 100 per cent of its stellar mass), but rescaled to the age of the Universe at the redshift of each galaxy.

The average of these three single addenda in the equation is allowed to vary from 0 to 1, with 1 denoting systems that have formed the totality of their stellar mass in the shortest possible time.[11] A higher DoR indicates an earlier formation epoch with almost no contribution from stars brought in through accretion or formed in later SF episodes. A lower DoR instead means that, although a fraction of stars are old and were formed at very high z, there is a non-negligible percentage (> 25 per cent, according to the DR1 threshold) of later formed populations with different ages and metallicities. Hence galaxies with low DoR are characterized by a much more time-extended SFH. However, it is important to stress that the definition of the DoR, linearly combining the $f_{M^{\star}_{t\mathrm{BB}=3}}$, the t_{75} (middle), and the $(t_{\mathrm{Uni}} - t_{\mathrm{fin}})/t_{\mathrm{Uni}}$ is motivated only by the stellar population analysis and the choices made in `INSPIRE` DR1.

We caution the reader that a one-to-one comparison between the relic definition in `INSPIRE` DR1 and this updated one is not straightforward. In fact, in DR1, we analysed two 1D extracted spectra for each galaxy (R50 and optimally extracted, see Spiniello et al. 2021b for more details) and considered the mean (lower limits for the) fraction of mass and t_{75} when classify UCMGs in relics and non-relics. Nevertheless, a direct comparison between the ages and metallicities obtained in the two DRs is presented in Appendix A. Overall, a very good agreement is found, with only two galaxies presenting different stellar population parameters: J0226−3158, which is ∼4 Gyr younger now, and J0316−2953 for which the metallicity is lower in this DR3 with respect to the supersolar value inferred in DR1. J0226−3158 is the only object for which the relic classification has dramatically changed in this DR3. In DR1 we inferred a mean $f_{M^{\star}_{t\mathrm{BB}=3}}$ of 0.685, while now the fraction went down to 0.09 ± 0.3. For the four extreme relics already presented in DR1, nothing has changed here: they have still formed the great majority of their stars ($f_{M^{\star}_{t\mathrm{BB}=3}}$>0.99) at $z > 2$.

In a forthcoming publication, already in preparation, we will use a more sophisticated machine-learning-based grouping algorithm to identify 'families' within the 52 UCMGs. We will feed the code with the morphological, photometrical, kinematical, and stellar population parameters searching for clustering and grouping, and then comparing these results with the DoR grading.

Fig. 6 shows the DoR defined above plotted versus the $f_{M^{\star}_{t\mathrm{BB}=3}}$ (top), the t_{75} (middle), and the $(t_{\mathrm{Uni}} - t_{\mathrm{fin}})/t_{\mathrm{Uni}}$ (bottom). The coloured regions in the first two panels identify the zone where non-relics (blue), relics (red), and extreme relics (magenta) will lie, following the `INSPIRE` DR1 approach. The same colour code as in DR1 is used in these panels. However, from the figure, it appears that the definition used in DR1 does not allow one to really appreciate the diversity of the 52 UCMGs, spanning different final times and fractions of masses formed at high z. For instance, the objects that would not pass the threshold of $f_{M^{\star}_{t\mathrm{BB}=3}}$≥0.75 cover a very large

---

[11] As a reference, NGC1277, the most extreme relic known so far in the local Universe, has a DoR of ∼0.95.

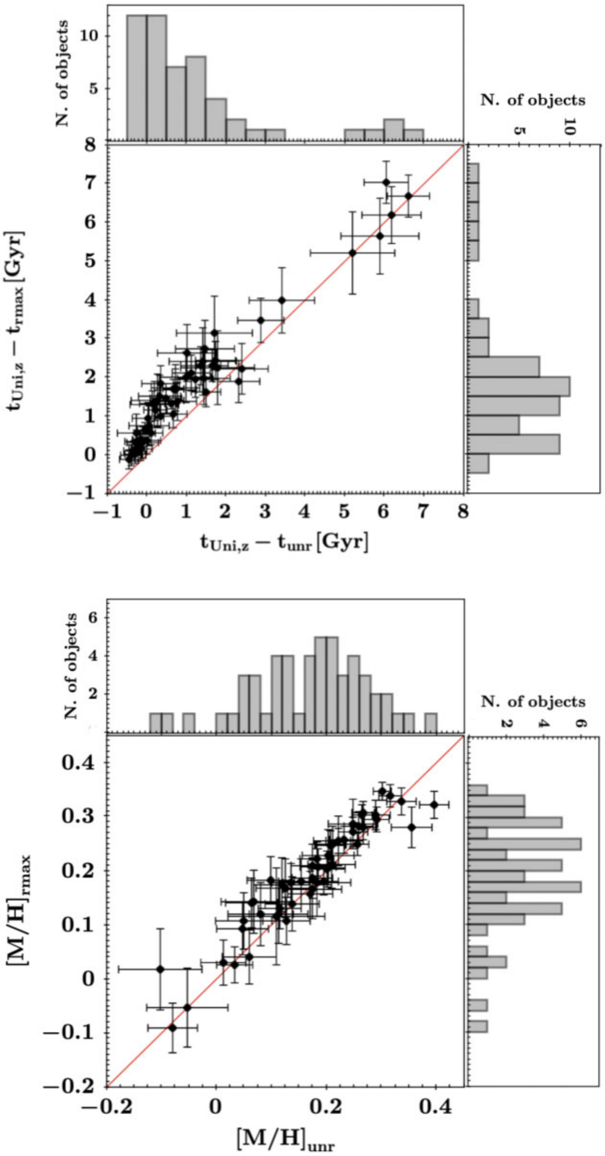

Figure 5. Scatter plots of the formation ages (top) and stellar metallicities (bottom) derived from the unr versus the rmax PPXF fits. As expected, ages are younger in the latter case. The points on the metallicity plot (lower panel) lie on the one-to-one line, shown in red. The histograms show the distribution of the parameters in the two cases separately.

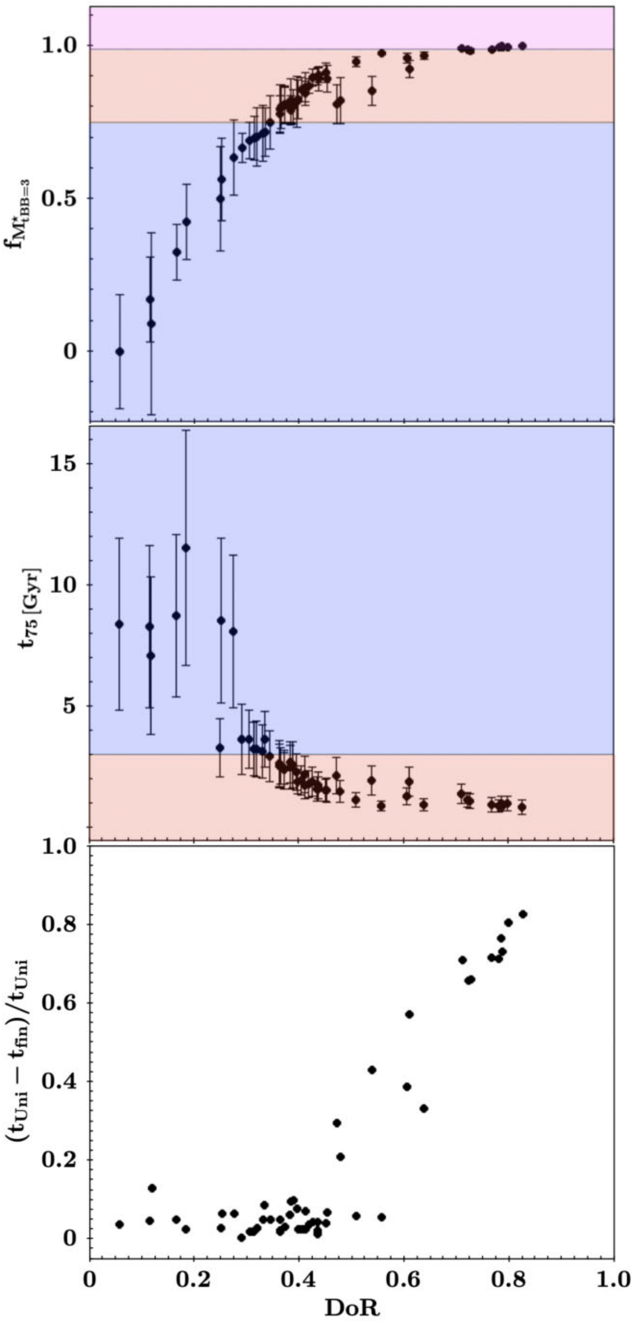

Figure 6. The DoR versus the fraction of mass formed up to 3 Gyr after the big bang (top), the cosmic time at which the galaxy have formed 75 per cent of their stellar mass (middle), and the time of final assembly (bottom). The horizontal lines show the thresholds corresponding to extreme relics (purple zone, upper plot) and relics (blue and red regions, first two plots) used in DR1.

range of fraction of mass formed at high z, from 0.72 ± 0.09 to as little as 0.00 ± 0.18. Also, some of them have t_{75} only slightly larger than 3 Gyr, while some others have much larger values. This is also valid for the final assembly time and objects that have been classified as relics in DR1. In conclusion, the DoR is a much robust and informative way to quantify the fraction of mass formed at early times and the SFHs for all the UCMGs in the `INSPIRE` sample.

Nine out of the 52 systems stand out from the overall distribution, having DoR$>$0.7, which translates into very high fractions of mass formed within 3 Gyr from the BB ($>$0.98), and very short t_{75} ($\leq$1.5) and $t_{\rm fin}$ ($\leq$3.5). These are clearly the most extreme cases: they were completely formed 3 Gyr after the big bang. On the other extreme of the distribution, seven UCMGs have formed 75 per cent of their stellar mass in a much longer time ($t_{75} > 7$ Gyr), and therefore they cannot be considered relics of the ancient Universe. The remaining 36 systems span a large range of DoR (0.25 $<$DoR$<$0.7).

Fig. 7 shows the cumulative fraction of mass formed in cosmic time since the BB for the unregularized case (top) and the one with the maximum regularization (bottom) for the entire `INSPIRE` sample.The galaxies are colour-coded by their DoR, as indicated in the coloured bar on the top. The figure highlights how different the SFHs of the 52 UCMGs are. All systems with DoR $\geq$ 0.7 (red and orange lines) have completely assembled their mass a couple of

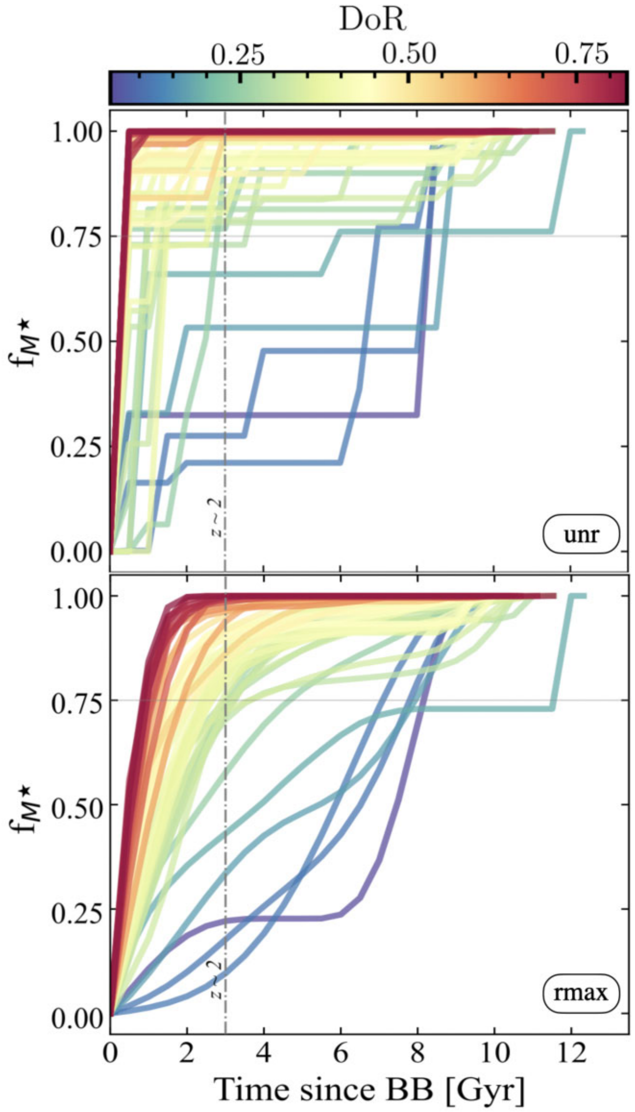

Figure 7. Cumulative fractions of mass formed in cosmic time since the BB for the unr (top) and the rmax (bottom) case for the entire `INSPIRE` sample. The galaxies are colour-coded by DoR.

Gyr from the BB. These can be considered extreme relics. Moving towards lower and lower DoR, the distribution of $f_{M^\star_{t\mathrm{BB}=3}}$ becomes instead more heterogeneous, in both the top and bottom panels. Interestingly, a similar diversity in the SFHs has also very recently been extended to compact galaxies at lower masses. For instance, Grèbol-Tomàs, Ferré-Mateu & Domínguez-Sánchez (2023) recently computed SFHs and formation time-scales of compact galaxies with $9.9 \leq \log{(M_\star/\mathrm{M}_\odot)} \leq 10$ from the Mapping Nearby Galaxies at APO (MaNGA) Survey (Bundy et al. 2015). Using a machine learning grouping algorithm, they found three clearly distinct groups: galaxies that have remained mostly unchanged since their early formation epoch, galaxies with a more extended and continuous SF, and galaxies with an initial very low star-forming rate that than increases with time.

5.2 Relic characterization

The corner plot of Fig. 8 shows the results of the stellar population analysis once all galaxies have been colour-coded by their DoR, as defined above. Extreme relics with DoR > 0.7 are plotted in red, while galaxies with a more extended SFH (i.e. non-relics, DoR < 0.25) are plotted in blue. This is in line with the colour-coding used in previous `INSPIRE` publications, but much more flexible. By construction, a higher DoR implies a lower t_{fin} and a higher $f_{M^\star_{t\mathrm{BB}=3}}$, i.e. an earlier final assembly with a higher fraction of stellar mass formed at $z > 2$. Clearly, this also means that galaxies with higher DoR have older integrated ages, as visible from the plot.

The 52 `INSPIRE` UCMGs span a large range in stellar velocity dispersion (∼130–400 km s^{-1}). For normal-sized galaxies, it is well known that the stellar population parameters and the SFHs correlate with it, in the sense that galaxies with higher $\sigma_\star$ have overall older integrated ages and larger metallicities (e.g. McDermid et al. 2015). This is true also for UCMGs.[12] However, we note that the definition of relics based on the cumulative mass fraction assembled in cosmic time does not directly depend on the stellar population parameters: UCMGs with very similar velocity dispersion (and also similar integrated age and metallicity) can have very different DoR (e.g. J1228−0153 with DoR $= 0.39$, $\sigma_\star = 191 \pm 10$ and J1438−0127 with DoR $= 0.78$, $\sigma_\star = 218 \pm 11$).

An interesting result, which confirms what was already hinted at in `INSPIRE` DR1, is that while galaxies with low DoR values are uniformly distributed around $\sigma \sim 200$–240 km s^{-1}, there is a high fraction of UCMGs with high DoR that have larger $\sigma_\star$. This means that the stellar velocity dispersion can potentially be used, in the future, to select the most reliable relic candidates among UCMGs (see e.g. Saulder, van den Bosch & Mieske 2015).

Fig. 9 shows the stellar mass versus the stellar velocity dispersion. The galaxies are colour-coded by their DoR, as in the previous figure. We have already shown in fig. 12 of `INSPIRE` DR1 and fig. 10 of `INSPIRE` DR2 that at equal stellar mass, relics tend to have, on average, larger stellar velocity dispersion values than non-relics and than normal-sized galaxies. Here, we do not wish to compare normal-sized galaxies with UMCGs, but only galaxies of very similar sizes but different DoR. Due to the larger number statistics, we now see that although some of the less extreme relics (i.e. yellow and orange points, with DoR∼0.3–0.6) have similar $\sigma_\star$ than non-relics of similar stellar mass and size, the majority of the systems with DoR>0.7 (red points) have larger velocity dispersions. Being the $\sigma_\star$ a proxy for the total mass of a system, given the virial theorem, and since all the plotted galaxies have very similar sizes and stellar masses, this plot implies that objects with a high DoR have larger mass-to-light ratios than objects with lower DoR. One of the possible physical motivations for this could be the fact that these objects are characterized by a steeper low-mass end of the IMF slope, since dwarf stars contribute substantially to the mass but only add a few per cent to the optical light (Conroy 2013). This seems to be the case, as we showed in Martín-Navarro et al. (2023), although with very limited number statistics (five relics and five non-relics). Alternatively, relics could have more dark matter or dark haloes with a higher central mass density. However, this seems to be in strong contrast with recent results showing that NGC1277, one of the three very well-studied extreme relics in the local Universe,

---

[12] Comparing relics and their properties with ATLAS$^{\mathrm{3D}}$ normal-sized galaxies of similar masses (e.g. fig. 22 in Cappellari 2016), the `INSPIRE` objects seems to have exactly the stellar population characteristics that one would expect by extrapolating the parameters of normal-sized ETGs beyond the ZoE. At equal stellar masses, smaller galaxies are older, have larger stellar velocity dispersion values, richer metallicities, and higher [α/Fe]. Relics are the extreme tails of these distributions.

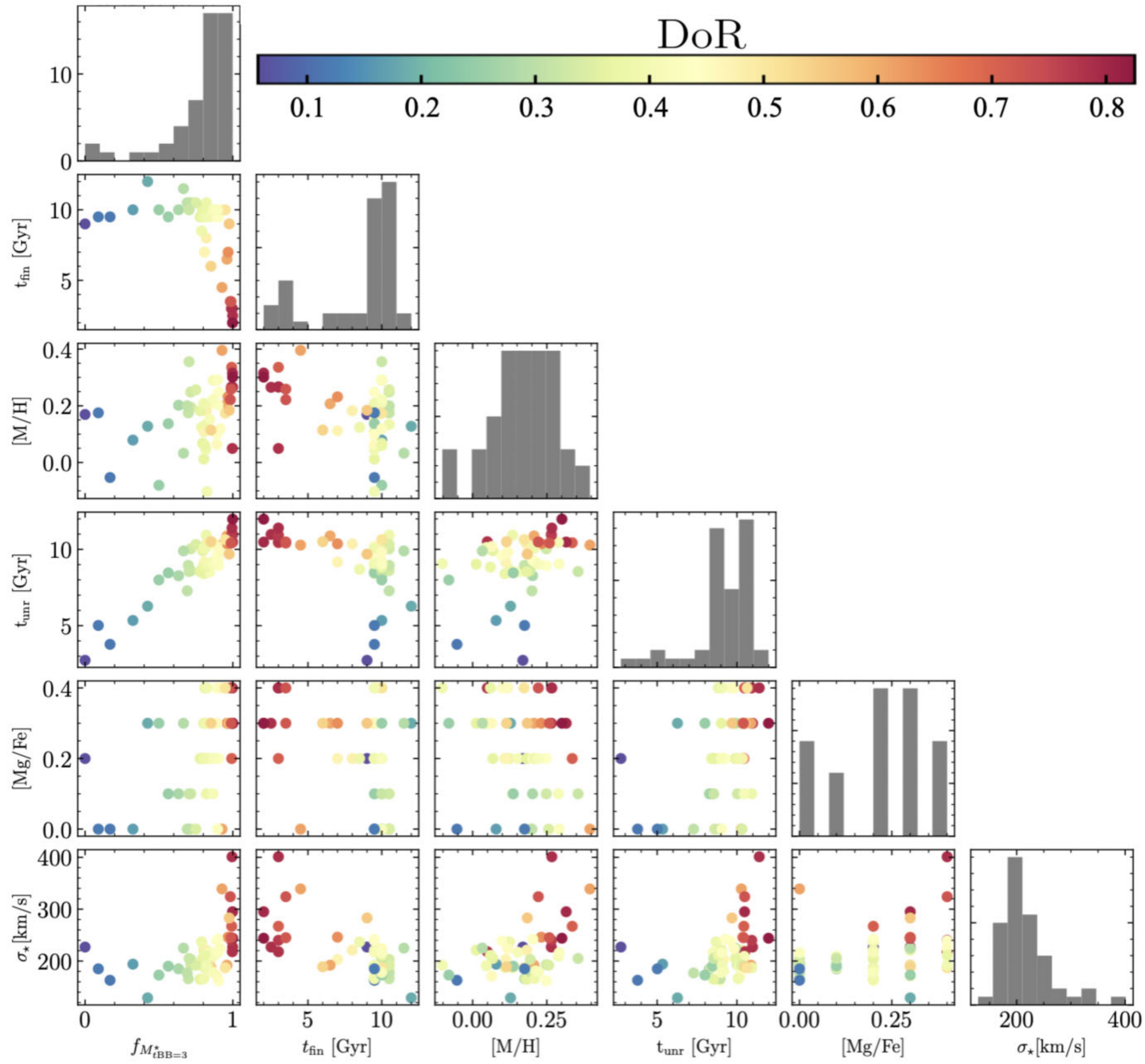

Figure 8. Correlation between the stellar population parameters. The `INSPIRE` galaxies are colour-coded by the DoR, with red being the most extreme relics and blue indicating objects with a relatively more extended SFH. Galaxies with higher DoR are older (by definition), more metal-rich, and have higher [Mg/Fe] ratios and velocity dispersion values.

is dark-matter-deficient up to 5 R_e (Comerón et al. 2023). We will tackle this problem in future dedicated publications (i) precisely constraining the IMF and (ii) performing a detailed dynamical model of the galaxies in the `INSPIRE` final sample. We finally note that it is not surprising that we do not find extreme relics at very high masses, as it is very rare for such massive galaxies to form in such short time-scales.

6 SUMMARY AND CONCLUSIONS

In this paper, we have presented the complete sample of the Investigating Stellar Populations In RElics (`INSPIRE`) Survey. The goal of `INSPIRE` has been to study the kinematics and stellar population parameters of a sample of UCMGs with effective radii $R_e < 2$ kpc and stellar masses $M_\star > 6 \times 10^{10}$ $M_\odot$ to build the first sizeable catalogue of spectroscopically confirmed relics at $0.1 < z < 0.4$. Observations were based on an ESO Large Program, which was completed in 2023 March. The data have been made available to the community through three ESO Data Releases (DR1: Spiniello et al. 2021b, DR2: D'Ago et al. 2023), the last of which has been described in this paper.

For each of the 52 UCMGs we have derived highly accurate spectroscopic redshifts, precise estimates of the integrated stellar velocity dispersion and the associated uncertainties, 'SSP-equivalent' [Mg/Fe] from line-indices and mass-weighted stellar ages, and metallicities from full-spectral fitting. All these quantities are released in a publicly available catalogue, together with morpho-photometric characteristics derived from KiDS and VIKING multiband images.

In this paper, we have:

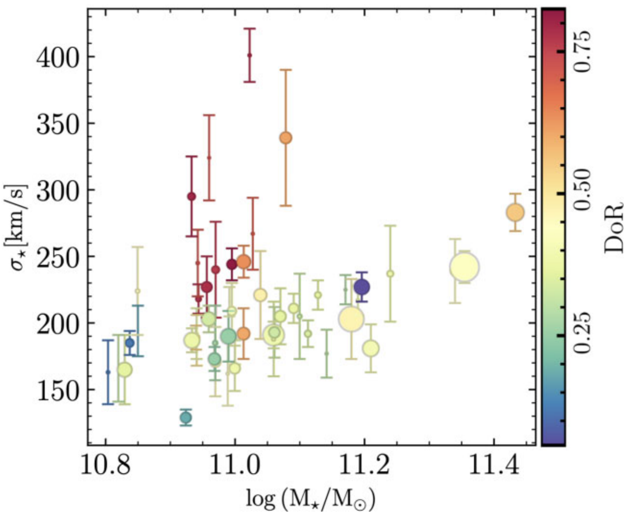

Figure 9. The $M_\star$–σ relation for the `INSPIRE` sample. Galaxies are colour-coded by their DoR and the symbol size scales with the R_e . Objects with a high DoR (red) have overall larger stellar velocity dispersion compared to galaxies with lower DoR but equal stellar mass.

(i) added 12 new, still unpublished systems to the previous DRs, releasing their UVB, VIS, and NIR spectra, as well as the combined spectrum smoothed at a resolution of FWHM=2.51 Å, that of the SSP models. All spectra have been extracted from an aperture that encapsulates 50 per cent of the light, but that takes into account that the data are seeing-dominated,

(ii) (re-)computed the stellar velocity dispersion ($\sigma_\star$) for all the `INSPIRE` galaxies using the code PPXF with a uniform configuration,

(iii) obtained stellar ages, metallicities, and [Mg/Fe] abundances for 33 new systems (DR2 and DR3) and for the 19 systems already presented in DR1 from the smoothed 1D UVB + VIS spectra.

These quantities allowed us to derive the SFHs of the galaxies in the entire `INSPIRE` sample and hence define, for each of the UCMGs, a DoR, based on the fraction of stellar mass assembled 3 Gyr after the BB ($z \geq 2$), on the time at which the galaxy had formed 75 per cent of its stellar mass and on the cosmic time of final assembly (100 per cent of the stellar mass formed), taking into account the redshifts of the systems. The DoR is defined as a dimensionless value that varies from 1 (the most extreme case: a galaxy that has fully assembled 700 Myr after the BB) to 0 (a galaxy that is still forming stars today).

Among the 52 `INSPIRE` UCMGs, nine can be defined as ‘extreme relics’, since they had formed >99 per cent of their stellar mass by $z = 2$, corresponding to a DoR>0.7. According to the simpler definition given in `INSPIRE` DR1, 38 objects would be classified as relics, having formed more than 75 per cent of their stellar mass by $z = 2$ ($0.34 \leq$DoR≤ 0.64). This number nicely confirms (and even increases) the initial expectation of the survey which predicted that 50 per cent of the sample would be classified as relic, following this simple, operational definition. However, here, in this final data release, we have defined a much more informative classification of these UCMGs, assigning a DoR to each system, that takes into account these SFH parameters in a roubst way. The DoR is found to correlate with the stellar velocity dispersion, [Mg/Fe], metallicity, and (by construction) age.

Among the 38 relics, the different DoR represents different SFHs, with some systems that have formed all their stars just 2 Gyr after the big bang (extreme, *DoR* > 0.7) and some others with much longer $t_{\rm fin}$ ($0.34 \leq$ DoR ≤ 0.64). The remaining 14 UCMGs are instead systems that are still forming stars or that stopped much later on in cosmic time. These objects could pose problems to simulations that will have to explain the presence of multiple SF episodes but a lack of growth. We note however that these systems, or at least a fraction of them, could also be ‘stripped’ objects that were much bigger in size but then lost part of their materials. Unfortunately with ground-based observations and `INSPIRE` integrated and seeing-dominated spectra we cannot disentangle between these cases.

In conclusion, the `INSPIRE` Survey has successfully built a sizeable catalogue of relics and younger UCMGs, which is released to the community. This opens up the opportunity to study in great detail the first phases of formation and mass assembly of massive galaxies at high z, but with the ease of being in the nearby Universe.

ACKNOWLEDGEMENTS

CS, CT, FLB, DB, PS, AG, and SZ acknowledge funding from the INAF PRIN-INAF 2020 program 1.05.01.85.11. AFM acknowledges support from RYC2021-031099-I and PID2021-123313NA-I00 of MICIN/AEI/10.13039/501100011033/FEDER,UE,NextGenerationEU/PRT. DS is supported by JPL, which is operated under a contract by Caltech for NASA. The authors wish to thank the ESO Archive Science Group for the great support with the Data Release.

DATA AVAILABILITY

The data described in this paper are publicly available via the ESO Phase 3 Archive Science Portal under the collection `INSPIRE` (https://archive.eso.org/scienceportal/home?data_collection = INSPIRE).

REFERENCES

Bennett C. L., Larson D., Weiland J. L., Hinshaw G., 2014, ApJ, 794, 135
Buitrago F. et al., 2018, A&A, 619, A137
Bundy K. et al., 2015, ApJ, 798, 7
Cappellari M., 2016, ARA&A, 54, 597
Cappellari M., 2017, MNRAS, 466, 798
Cappellari M., Emsellem E., 2004, PASP, 116, 138
Carnall A. C. et al., 2023, MNRAS, 520, 3974
Charbonnier A. et al., 2017, MNRAS, 469, 4523
Comerón S. et al., 2023, A&A, 675, A143
Conroy C., 2013, ARA&A, 51, 393
Conroy C., van Dokkum P. G., 2012, ApJ, 760, 71
D’Ago G. et al., 2023, A&A, 672, A17
Damjanov I., Abraham R. G., McCarthy P. J., Glazebrook K., 2009, in American Astronomical Society Meeting Abstracts #213. p. 512
Damjanov I., Chilingarian I., Hwang H. S., Geller M. J., 2013, ApJ, 775, L48
Damjanov I., Hwang H. S., Geller M. J., Chilingarian I., 2014, ApJ, 793, 39
Damjanov I., Geller M. J., Zahid H. J., Hwang H. S., 2015a, ApJ, 806, 158
Damjanov I., Zahid H. J., Geller M. J., Hwang H. S., 2015b, ApJ, 815, 104
de Jong J. T. A. et al., 2015, A&A, 582, A62
de Jong J. T. A. et al., 2017, A&A, 604, A134
Edge A., Sutherland W., K., Kuijken S. Driver R. McMahon S. Eales J.~P. Emerson, 2013, The Messenger, p. 154, 32
Eftekhari E., La Barbera F., Vazdekis A., Allende Prieto C., Knowles A. T., 2022, MNRAS, 512, 378
Ferré-Mateu A., Trujillo I., Martín-Navarro I., Vazdekis A., Mezcua M., Balcells M., Domínguez L., 2017, MNRAS, 467, 1929
Freudling W., Romaniello M., Bramich D. M., Ballester P., Forchi V., García-Dabló C. E., Moehler S., Neeser M. J., 2013, A&A, 559, A96

Gallazzi A., Charlot S., Brinchmann J., White S. D. M., 2006, MNRAS, 370, 1106

Gallazzi A. R., Pasquali A., Zibetti S., Barbera F. L., 2021, MNRAS, 502, 4457

Grèbol-Tomàs P., Ferré-Mateu A., Domínguez-Sánchez H., 2023, MNRAS, 526, 4024

Guo Q. et al., 2011, MNRAS, 413, 101

Guo Q., White S., Angulo R. E., Henriques B., Lemson G., Boylan-Kolchin M., Thomas P., Short C., 2013, MNRAS, 428, 1351

Huertas-Company M. et al., 2016, MNRAS, 462, 4495

Knowles A. T., Sansom A. E., Vazdekis A., Allende Prieto C., 2023, MNRAS, 523, 3450

Kuijken K., 2011, The Messenger, 146, 8

La Barbera F., de Carvalho R. R., Kohl-Moreira J. L., Gal R. R., Soares-Santos M., Capaccioli M., Santos R., Sant'anna N., 2008, PASP, 120, 681

La Barbera F., Ferreras I., Vazdekis A., de la Rosa I. G., de Carvalho R. R., Trevisan M., Falcón-Barroso J., Ricciardelli E., 2013, MNRAS, 433, 3017

Labbé I. et al., 2023, Nature, 616, 266

Lisiecki K., Małek K., Siudek M., Pollo A., Krywult J., Karska A., Junais, 2023, A&A, 669, A95

Liu Y., 2020, MNRAS, 497, 3011

Martín-Navarro I., Vazdekis A., Falcón-Barroso J., La Barbera F., Yıldırım A., van de Ven G., 2018, MNRAS, 475, 3700

Martín-Navarro I. et al., 2023, MNRAS, 521, 1408

Matteucci F., 1994, A&A, 288, 57

McDermid R. M. et al., 2015, MNRAS, 448, 3484

Naab T., Johansson P. H., Ostriker J. P., 2009, ApJ, 699, L178

Naab T. et al., 2014, MNRAS, 444, 3357

Nanayakkara T. et al., 2022, preprint (arXiv:2212.11638)

Oser L., Ostriker J. P., Naab T., Johansson P. H., Burkert A., 2010, ApJ, 725, 2312

Pietrinferni A., Cassisi S., Salaris M., Castelli F., 2004, ApJ, 612, 168

Pietrinferni A., Cassisi S., Salaris M., Castelli F., 2006, ApJ, 642, 797

Poggianti B. M. et al., 2013, ApJ, 762, 77

Quilis V., Trujillo I., 2013, ApJ, 773, L8

Roy N. et al., 2018, MNRAS, 480, 1057

Salvador-Rusiñol N., Beasley M. A., Vazdekis A., Barbera F. L., 2021, MNRAS, 500, 3368

Salvador-Rusiñol N., Ferré-Mateu A., Vazdekis A., Beasley M. A., 2022, MNRAS, 515, 4514

Sánchez-Blázquez P., Gorgas J., Cardiel N., 2006, A&A, 457, 823

Sanders R. H., 2014, MNRAS, 439, 1781

Saulder C., van den Bosch R. C. E., Mieske S., 2015, A&A, 578, A134

Scognamiglio D. et al., 2020, ApJ, 893, 4 (S20)

Smette A. et al., 2015, A&A, 576, A77

Spiniello C., Trager S., Koopmans L. V. E., Conroy C., 2014, MNRAS, 438, 1483

Spiniello C. et al., 2021a, A&A, 646, A28

Spiniello C. et al., 2021b, A&A, 654, A136

Stoehr F. et al., 2008, in Argyle R. W., Bunclark P. S., Lewis J. R., eds, ASP Conf. Ser. Vol. 394, Astronomical Data Analysis Software and Systems XVII. Astron. Soc. Pac., San Francisco, p. 505

Thomas D., Maraston C., Bender R., Mendes de Oliveira C., 2005, ApJ, 621, 673

Tortora C. et al., 2016, MNRAS, 457, 2845

Tortora C. et al., 2018, MNRAS, 481, 4728 (T18)

Trager S. C., Faber S. M., Dressler A., 2008, MNRAS, 386, 715

Trujillo I., Cenarro A. J., de Lorenzo-Cáceres A., Vazdekis A., de la Rosa I. G., Cava A., 2009, ApJ, 692, L118

Trujillo I., Carrasco E. R., Ferré-Mateu A., 2012, ApJ, 751, 45

Trujillo I., Ferré-Mateu A., Balcells M., Vazdekis A., Sánchez-Blázquez P., 2014, ApJ, 780, L20

Vazdekis A. et al., 2015, MNRAS, 449, 1177

Vazdekis A., Koleva M., Ricciardelli E., Röck B., Falcón-Barroso J., 2016, MNRAS, 463, 3409

Vernet J. et al., 2011, A&A, 536, A105

Yıldırım A., van den Bosch R. C. E., van de Ven G., Husemann B., Lyubenova M., Walsh J. L., Gebhardt K., Gültekin K., 2015, MNRAS, 452, 1792

Yıldırım A., van den Bosch R. C. E., van de Ven G., Martín-Navarro I., Walsh J. L., Husemann B., Gültekin K., Gebhardt K., 2017, MNRAS, 468, 4216

Zolotov A. et al., 2015, MNRAS, 450, 2327

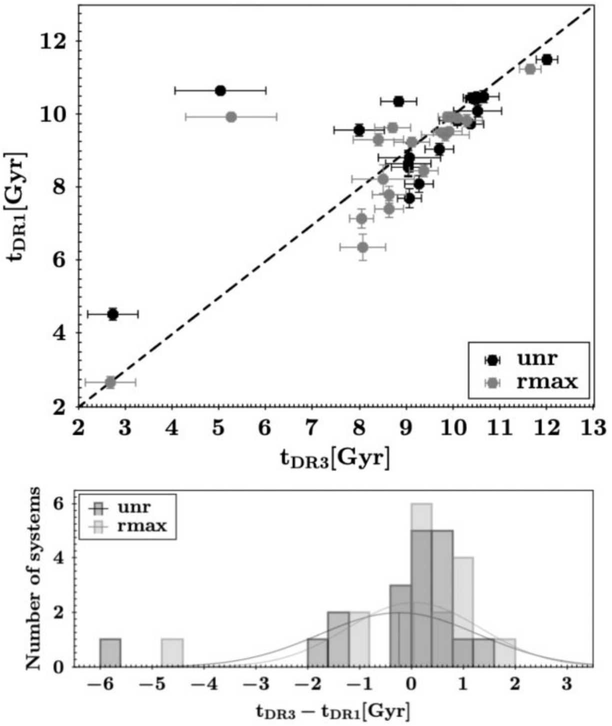

Figure A1. Comparison between DR3 and DR1 stellar ages. The top panel shows the scatter plot, with the one-to-one relation shown as a dotted line. The bottom panel shows the histogram of the difference between the two values. The different colours indicate the unr and the rmax estimates.

APPENDIX A: COMPARISON WITH DR1

In this appendix, we show a direct comparison between the stellar population results obtained in DR1 (Spiniello et al. 2021b) and those presented here for 19 objects. For consistency, we only consider here the optimally extracted spectra from DR1, the only one we use in this DR3.

Here, below we briefly list the main (small) differences between DR1 and this paper.

(i) *Fitting region:* in DR1, we restrict the fit to the spectral region [3500–7000] Å, while here we go slightly redder, up to 7500 Å. The spectral range used for the fit does play a role both in measuring the velocity dispersion (see the tests in INSPIRE DR2) and in determining the SFHs for a couple of systems with low DoR. This is probably caused by the presence of a noisy region around 7100–7200 Å for them (this is also visible from the bottom panel of Fig. 4), showing J2327−3312, the youngest galaxy in the INSPIRE sample. However, this does not affect the main conclusions or the classification obtained in the paper.

(ii) pPXF *version:* the version 7.4 was used in DR1, whereas version 8.2.4 is used in this paper.

(iii) *Cleaning and masking:* we slightly improve the masking of bad pixel regions and additionally used the CLEAN keyword in pPXF.

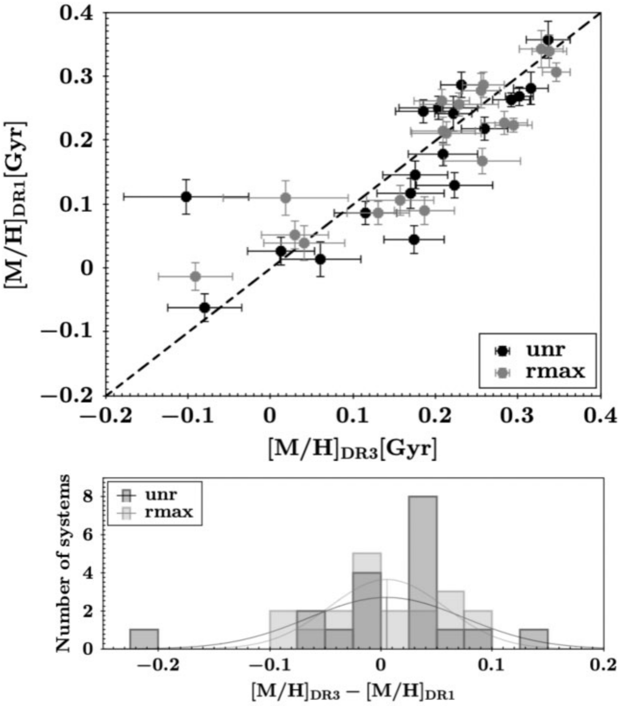

Figure A2. Same as in Fig. A1 but with the metallicity estimates.

Overall, a fair agreement is found for the majority of the systems for both age and metallicity, with however a small systematic effect towards slightly older ages, as shown in the top panels of Figs A1 and A2. The bottom panels of each plot the histograms of the difference between the age and metallicity computed in the two DRs. For both the unr and the rmax cases, a Gaussian fit to the difference shows no systematic differences and a spread of about 1–2 Gyr for the age and of ∼−0.1 for [M/H]. With the exception of two galaxies:

(i) **J0226−3158**. For this galaxy, a much older stellar age was inferred (∼10 Gyr) in DR1, compared with the one we infer here (∼6 Gyr), for both the unregularized and the regularized cases.

(ii) **J0316−2953**. For this galaxy, the age estimates agree within 1.5σ (with the ones estimated here being ∼1 Gyr older), but the inferred [M/H] values differ by 0.2 dex. In DR1 J0316−2953 resulted to be slightly supersolar, while here it has [M/H] values below solar now with the new analysis. The disagreement is however smaller when considering the rmax case.

APPENDIX B: UCMGS AND RELICS NUMBER DENSITY

With the final `INSPIRE` sample at our disposal and the relic confirmation described above, we can update the lower limit to the number density of relics (and UCMGs) obtained in previous DRs. This number provides an important constraint for galaxy assembly models and simulations.

Following the approach of T18, already used also in `INSPIRE` DR1, the number density is defined as

$$\rho = \frac{f_{\mathrm{area}} \times N_{\mathrm{conf}}}{V_{\mathrm{KiDS,z}}}, \tag{B1}$$

where N_{conf} is the number of objects. We considered both the 38 systems that have $f_{M^{\star}_{t\mathrm{BB}=3}} \geq 0.75$ and the entire sample of 52 UCMGs. The $V_{\mathrm{KiDS,\,z}}$ is the cosmic comoving volume contained within the redshift window covered by `INSPIRE` ($0.1 < z < 0.41$), and is calculated as follows: $V_{\mathrm{KiDS,\,z}} = (V_{z\,=\,0.41} - V_{z\,=\,0.1})$. Finally, f_{area} is a normalization factor used to normalize the number of objects to the full sky area. It is defined as the ratio $A_{\mathrm{sky}}/A_{\mathrm{KiDS}}$, where $A_{\mathrm{sky}} = 41\,253\ \mathrm{deg}^2$ is the full sky area and $A_{\mathrm{KiDS}} = 333\ \mathrm{deg}^2$ is the KiDS DR3 effective area within which the UCMGs are found (de Jong et al. 2017).

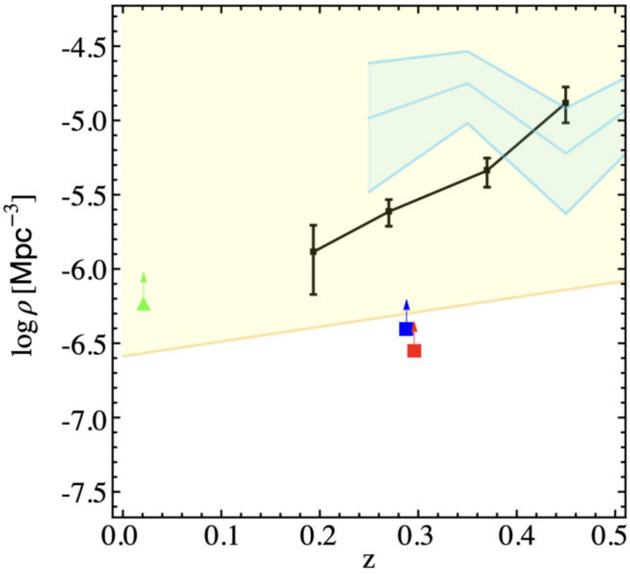

Figure B1. Number density of `INSPIRE` UCMGs (blue square) and relics ($f_{M^{\star}_{t\mathrm{BB}=3}} \geq 0.75$, red square) versus redshift. The black points and lines are the UMCGs from T18. The green triangle shows the lower limit inferred from the three local relics by Ferré-Mateu et al. (2017). The shaded yellow region highlights the region predicted by simulations. This has been computed as the lowest limit presented in Quilis & Trujillo (2013). The cyan line and region show the number counts for compact galaxies in the COSMOS area (Damjanov et al. 2015a).

The number density for the 38 relics (red point, $\log \rho \sim 2.8 \times 10^{-7}$ Mpc^{-3}) and the entire `INSPIRE` sample (blue point, $\log \rho \sim 3.9 \times 10^{-7}$ Mpc^{-3}) is shown in Fig. B1. This second value, although does not represent a benchmark for simulations wishing to compare the number of predicted relics, is useful for comparing our findings to the many works computing the number density of UCMGs, without any distinctions between old and younger systems (e.g. Tortora et al. 2018; Scognamiglio et al. 2020). In the same figure, we also show the lower limit estimated by Ferré-Mateu et al. (2017) from the three local relics (green triangle) and the trend inferred by T18 (black points) considering all UCMGs found in KiDS. The yellow region shows the zone predicted by Quilis & Trujillo (2013), who used the semi-analytical simulations from Guo et al. (2011) and Guo et al. (2013) to define 'relic compacts' galaxies with mass changing less than 10 per cent from $z \sim 2$. A mild evolution is found with redshift for all the mentioned studies. The cyan region and line represent the number densities from Damjanov et al. (2015a) inferred for galaxies in the COSMOS survey. In this case, no redshift evolution is found.

Our estimates are slightly below the value reported by F17 and the limit predicted by simulations. However, we stress that this number has to be considered as a lower limit on the relic number density, as the completeness and the selection function of the UCMGs/relics have not been taken into account.

APPENDIX C: 1D SPECTRA

In this appendix, we show the 1D R50 spectra for all the galaxies in the `INSPIRE` sample, ordered and divided by SNR group, as described in Section 3 and Table 2. In particular, Fig. C1 shows the spectra with mean SNR $>$ 35, Fig. C2 those with medium SNR (25 $<$ SNR $<$ 35), and Fig. C3 those with SNR ranging from 15 to 25. For display purposes, the spectra have been smoothed with a median filter with a nine-pixel width. There are two slightly noisy regions (around 4200 Å, and around 7200 Å) where the three arms have been joined together, and two very noisy ones, which correspond to the large telluric bands. All these have been masked out from the analysis of the stellar kinematics and populations. We remind the reader that, for this DR, the stellar population parameters have been constrained from the spectral region [3500–7500] Å. In this region, the SSP behaviour is solid and well studied; the influence of possible changes in the IMF slope and of very small ($<$ 1 per cent) SF residuals are negligible. In future `INSPIRE` papers we will focus more on the UVB and NIR regions.

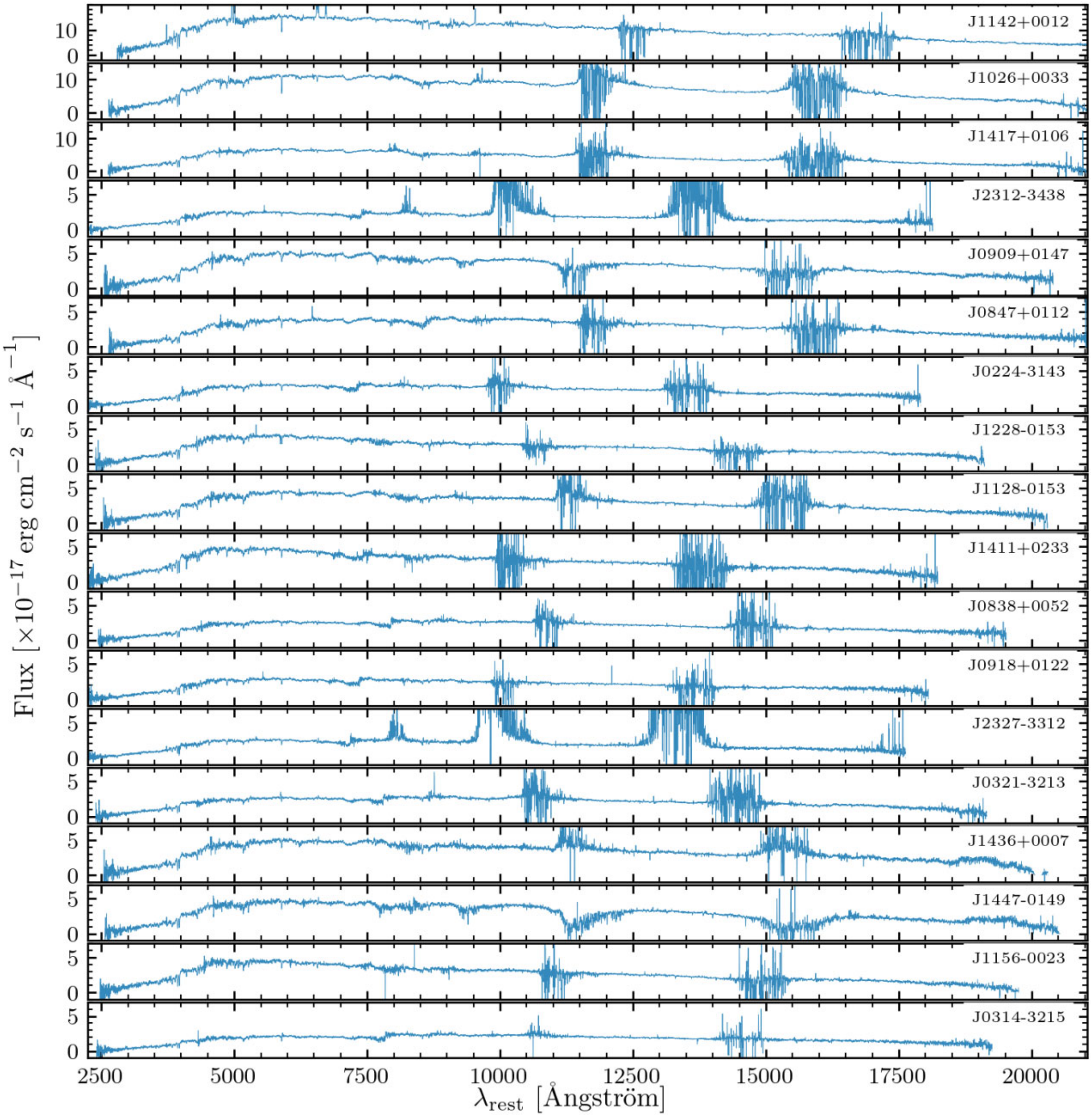

Figure C1. 1D smoothed spectra (9-pixel wide median filter) for the systems in the high SNR group (SNR $>$ 35). The single-arm spectra are joined together after restframing and rebinning to a final resolution of FWHM=2.51 Å. Residuals from telluric lines have not been removed from the spectra, but have been masked out for the kinematics and stellar population analysis.

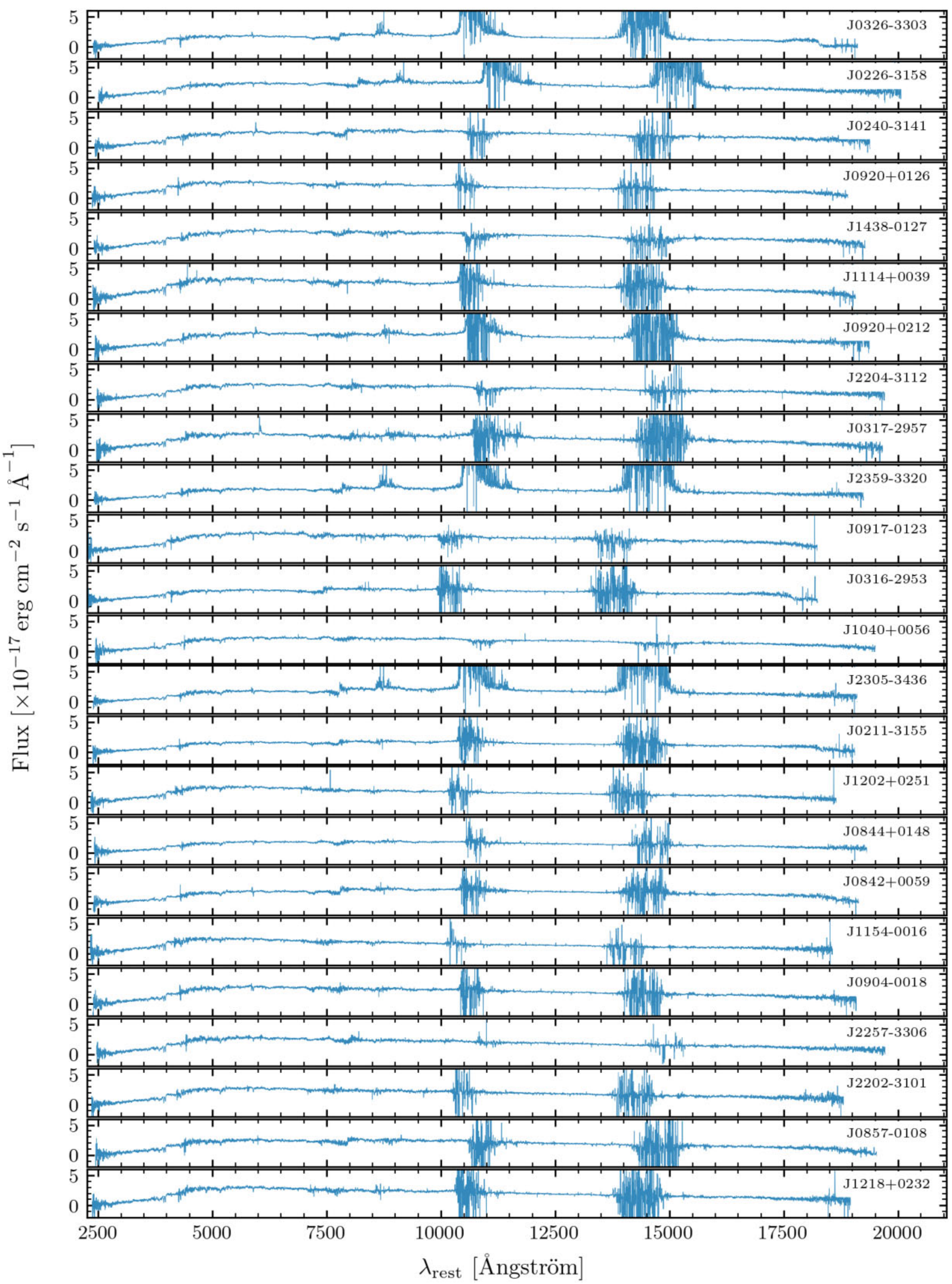

Figure C2. Same as the previous figure, but for the spectra in the medium SNR group (25 < SNR < 35).

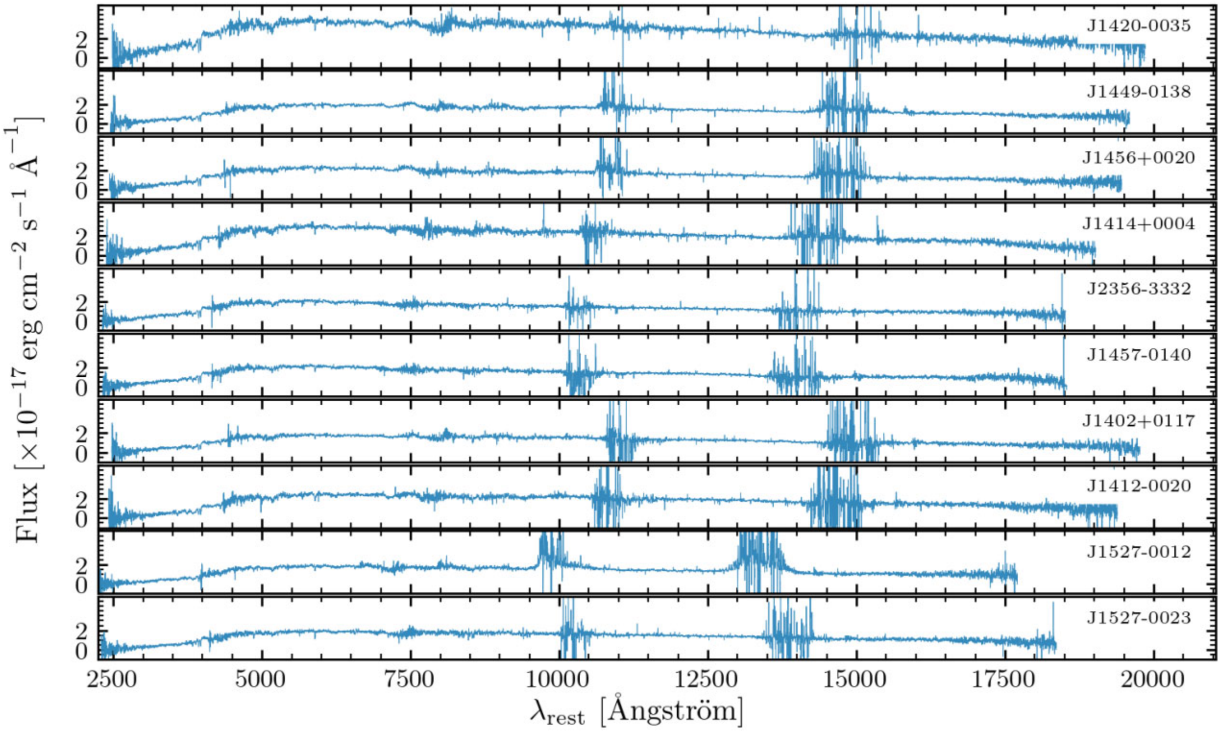

Figure C3. Same as the previous figure, but for the spectra in the low SNR group (SNR < 25).

This paper has been typeset from a TEX/LATEX file prepared by the author.